LA-UR-16-26524
Approved for public release; distribution is unlimited.

Title: A High-Rate, Single-Crystal Model including Phase Transformations, Plastic Slip, and Twinning

Author(s): Addessio, Francis L.; Bronkhorst, Curt Allan; Bolme, Cynthia Anne; Brown, Donald William; Cerreta, Ellen Kathleen; Lebensohn, Ricardo A.; Lookman, Turab; Luscher, Darby Jon; Mayeur, Jason Rhea; Morrow, Benjamin; Rigg, Paulo A

Intended for: Report

Issued: 2016-08-25

A High-Rate, Single-Crystal Model including Phase Transformations, Plastic Slip, and Twinning

F.L. Addessio[a], C.A.Bronkhorst[a], C.A. Bolme[c], D.W.Brown[b], E.K. Cerreta[b], R.A. Lebensohn[b], T. Lookman[a], D.J. Luscher[a], J.R. Mayeur [a], B.M. Morrow[b], P.A. Rigg[d]

[a]*Theoretical Division, Los Alamos National Laboratory, Los Alamos, NM 87545, USA*

[b]*Materials Science and Technology Division, Los Alamos National Laboratory, Los Alamos, NM 87545, USA*

[c]*Explosive Science and Shock Physics Division, Los Alamos National Laboratory, Los Alamos, NM 87545, USA*

[d]*Institute for Shock Physics and Department of Physics, Washington State University, Pullman, Washington 99164, USA*

Rough Draft (8/9/16)

LA-UR-xxxx

Blank Page

A High-Rate, Single-Crystal Model including Phase Transformations, Plastic Slip, and Twinning

F.L. Addessio[a], C.A.Bronkhorst[a], C.A. Bolme[c], D.W.Brown[b], E.K. Cerreta[b], R.A. Lebensohn[b], T. Lookman[a], D.J. Luscher[a], J.R. Mayeur [a], B.M. Morrow[b], P.A. Rigg[d]

[a]*Theoretical Division, Los Alamos National Laboratory, Los Alamos, NM 87545, USA*

[b]*Materials Science and Technology Division, Los Alamos National Laboratory, Los Alamos, NM 87545, USA*

Explosive Science and Shock Physics Division, Los Alamos National Laboratory, Los Alamos, NM 87545, USA

[d]*Institute for Shock Physics and Department of Physics, Washington State University, Pullman, Washington 99164, USA*

Abstract

An anisotropic, rate-dependent, single-crystal approach for modeling materials under the conditions of high strain rates and pressures is provided. The model includes the effects of large deformations, nonlinear elasticity, phase transformations, and plastic slip and twinning. It is envisioned that the model may be used to examine these coupled effects on the local deformation of materials that are subjected to ballistic impact or explosive loading. The model is formulated using a multiplicative decomposition of the deformation gradient. A plate impact experiment on a multi-crystal sample of titanium was conducted. The particle velocities at the back surface of three crystal orientations relative to the direction of impact were measured. Molecular dynamics simulations were conducted to investigate the details of the high-rate deformation and pursue issues related to the phase transformation for titanium. Simulations using the single crystal model were conducted and compared to the high-rate experimental data for the impact loaded single crystals. The model was found to capture the features of the experiments.

Keywords: Titanium, High-Strain Rate, Crystal Plasticity, Twinning, Phase Transformations

I. Introduction / Background

The ability to model high-rate deformations is important for addressing dynamic impact or explosive loading scenarios that are encountered in automotive, aerospace, and defense applications. The deformation characteristics at the meso-mechanical or single-crystal length scale have a direct effect on the macro-mechanical response of engineering structures. Therefore, it is important to understand the coupled role of plastic slip, twinning, and phase transformations at the meso-scale for high-rate conditions. The coupled effects of

the evolution of inelastic phenomena on the constitutive response of materials are poorly understood for dynamic conditions. Physically-based, meso-mechanical (~10 μm) models are necessary to guide macro-mechanical model development and assist in the interpretation of experimental data. Continuum single-crystal theories allow for the simulations of materials at the meso-scale. That is, length and time scales that are larger than allowed by atomistic approaches but at scales that provide a greater resolution and detail than considered by macro-mechanical or engineering models. Therefore, single-crystals models serve as a bridge between atomistic and macro-mechanical scales. Meso-mechanical models have proven to be capable of capturing the micro-mechanical phenomena that govern the deformation characteristics of materials.

There are numerous examples in the technical literature of investigations at the single-crystal length scale. Most of these efforts are focused on low-rate deformations of metallic materials due to plastic slip. The use of single-crystal models to examine the polycrystal response to deformations and the evolution of texture is ubiquitous. Crystal plasticity models have successfully explored coupled effects on the deformation characteristics of materials using computational simulations. Models that address the single-crystal response to high-rate deformations also are available. The dynamic behavior of materials is closely related to the microstructural evolution during the deformation process [Meyers (1994)]. For example, the high-rate, high pressure deformation of a single crystal to shock loading and the effect of a stress pulse on the nonuniform plastic deformation of a polycrystal sample of tantalum (Ta) has been considered [Becker ((2004)]. High-rate deformation and localization in Ta also has been addressed (Bronkhorst et al. (2007)]. Plate impact experiments and simulations using a dislocation-based, single-crystal model have been used to investigate the high-rate deformation of lithium fluoride (LiF) and copper (Cu) [Winey and Gupta (2006)] as well as quartz and sapphire [Winey and Gupta (2004)]. The high-rate deformation of energetic, organic single crystals also has received attention. The response to shocked pentaerythritol tetranitrate (PETN) [Winey and Gupta (2010)] and the α-polymorph of cyclotrimethylene trinitramine (RDX) has received recent attention [De et al. (2014; Luscher et al. (2016)]. The ability to include phase transformations for high-rate deformations also has been considered. A single-crystal model for the shock induced α (bcc) to ε (hcp) phase transformation in iron (Fe) was used to investigate the response of single crystals and an ensemble of single crystals to high-rate loading [Barton et al. (2005)] as well as the α (trigonal) to β (hex) transformation in quartz [Barton and Wenk (2007)].

Group-IV hexagonal-close-packed (hcp) metals [titanium (Ti), zirconium (Zr), and hafnium (Hf)] provide excellent candidates for studying high-rate deformations, because of their ability to deform plastically, twin, and phase transform at temperatures and pressures, which are relatively accessible. The inelastic behavior of these metals plays an important role in their physical properties and mechanical behavior. Toughness, ductility, spall strength and localization all are influenced by their inelastic response. Phase transformations in group-IV metals are martensitic-like in nature [Ivanisenko et al. (2008); Singh et al. (1982); Vohra (1978)]. That is, they are rapid, displacive, and diffusionless. It has been shown that applied shear strains may enhance the transformation kinetics [Ivanisenko et al. (2008); Zong et al. (2014)] of group-IV metals and their alloys. An apparent increase in the spall strength of alloys of these metals also has been observed [Mescheryakov and Divakov (2001)] depending on whether the reverse phase transformation occurs prior to the spallation event. In the past, polycrystal investigations using group-IV metals have been conducted for both quasi-static and high-rate conditions.

Hexagonal-close-packed (hcp) single crystals have been studied under static and dynamic pressures [Vohra (1978)]. Insight into the deformation mechanisms has been obtained from these investigations. However, fewer investigations for hcp single crystals have been pursued for high-strain rates, including phase transformations. Recently, high-rate, single-crystal plate impact [Cerreta et al. (2013)] and split-Hopkinson pressure bar (SHPB) experiments [Morrow et al. (2016)] were performed. When shocked above the α to ω transformation pressure, Zr samples that were recovered from single-crystal, plate impact experiments displayed a volume fraction of retained high-pressure phase (ω) that was related to the peak shock pressure [Cerreta et al. (2013)]. Quasi-static annealing experiments of the post-shocked, recovered Zr samples were conducted [Low et al. (2015)] to investigate the reverse transformation kinetics and the resulting evolution of dislocation densities in both the α and ω phases. The influence of the evolution of the microstructure on the reverse transformation was explored. In the SHPB experiments, single-crytals of Ti were loaded at high rate ($\dot{\varepsilon} \sim 4.45 \times 10^3$ s^{-1}], below the transformation pressure, and placed at different orientations with respect to the direction of compression. The samples were loaded to about 30 % strain. The mechanical response of the single crystals of Ti differed significantly as the orientation of the samples was changed relative to the compression direction. In addition to pursuing microscopy on the recovered samples, the evolution of the microstructure was investigated using a visco-plastic, self-consistent (VPSC) theory. It was determined that above ~ 10 % strain, the crystal that was compressed along the $[0001]$ orientation deformed primarily by compressive twinning. By ~25 % strain, the single crystal was completely twinned. However, the crystal that was compressed along the $[10\bar{1}1]$ orientation displayed significant prismatic slip [Morrow et al (2016)].

A thermo-mechanical framework for the large deformation of single-crystals [Turtletaub and Suiker (2006); Tjahjanto et al. (2008a); Tjahjanto et al. (2008b); Suiker and Turteltaub (2005); Suiker and Turteltaub (2007a); Suiker and Turteltaub (2007b)] has been developed. The original framework included the effects of linear elasticity, phase transformations, and plastic slip. The model relied on the multiplicative decomposition of the deformation gradient (F) into its elastic (F_{el}), plastic (F_{pl}), and transformation (F_{tr}) components

$$F = F_{el}\, F_{pl}\, F_{tr}\,. \tag{I-1}$$

The multiplicative decomposition of the deformation gradient is provided in schematic form in Fig. 1. It may be seen from Fig. 1 that the decomposition represents four configurations, the reference configuration ($\bar{b}$), two intermediate configurations ($\hat{b}$ *and* $\tilde{b}$), and the current configuration (b). The total deformation gradient ($\dot{F}\, F^{-1} = L$) may be determined directly from the velocity gradient (L), which is obtained from the solution to the momentum equations in the current configuration. The entropy density was considered to be a thermal analogue of the deformation gradient [Turteltaub et al. (2006)]. Therefore, analogous to the multiplicative decomposition of the total deformation gradient, the total entropy density ($\bar{\eta}$) was additively decomposed into its reversible ($\bar{\eta}_{el}$), plastic ($\bar{\eta}_{pl}$), and transformation ($\bar{\eta}_{tr}$) components

$$\bar{\eta} = \bar{\eta}_{el} + \bar{\eta}_{pl} + \bar{\eta}_{tr}\,. \tag{I-2}$$

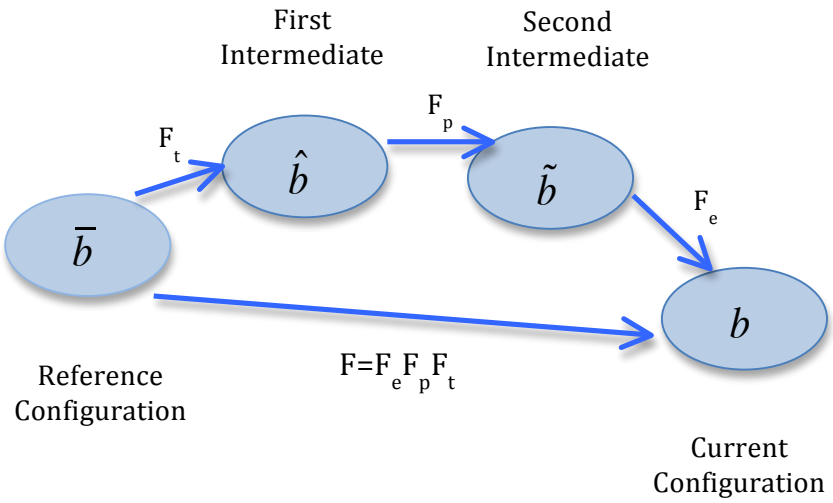

Fig. 1. Schematic figure of the decomposition of the Deformation Gradient

Micro-mechanical or sub-granular effects that are related to the internal structure of the crystal and the dislocation dynamics were treated in an averaged fashion. That is, it was assumed that the details of the micro-scale elastic, plastic, and transformation deformations were captured in an average sense by the decompositions of the deformation gradient and entropy density. In the development, it was assumed that the elastic deformation gradient ($F_{el}^{\phi} = F_{el}$) and the temperature ($\theta^{\phi} = \theta$) were uniform for each of the constituents (ϕ).

The transformation deformation gradient was based on lower-length scale (~1 μm) contributions that are included through crystallographic information that was derived from the theory of martensitic transformations [Ball and James (1987); James and Hane (2000); Bhattacharya (2007)]. That is, the jump in the stretch tensor across the habit plane between the parent and daughter phases was used to obtain the local jump condition for the deformation gradient for a transformation system (ω). The local jump condition then was volume averaged to provide a meso-mechanical (~10 μm) jump condition in terms of the effective transformation deformation gradient (F_{tr})

$$\begin{aligned} F_{tr} - I &= \sum_{\omega} \bar{\xi}^{\omega}\, \gamma_{tr} \left(b^{\omega} \otimes m^{\omega} \right) \equiv \sum_{\omega} \bar{\xi}^{\omega}\, T_{tr}^{\omega} \\ \dot{F}_{tr} &= \sum_{\omega} \dot{\bar{\xi}}^{\omega}\, T_{tr}^{\omega} \end{aligned} \quad . \qquad \text{(I-3)}$$

In Eq. (I-3), $\bar{\xi}^{\omega}$ is the volume fraction of the daughter constituents, γ_{tr} is the shape strain magnitude, which is related to the volume change for the transformation, b^{ω} is the shape strain vector, and m^{ω} is the normal to the habit plane. The sum in Eq. (I-3) is taken over the product constituents. The transformation deformation gradient is written in the reference configuration, which coincides with the low-pressure phase in the current application. The shape strain tensor (T_{tr}^{ω}) is assumed to remain constant in the reference configuration. The expression for the transformation entropy density was written [Turteltaub, et. al. (2006)]

$$\bar{\eta}_{tr} = \sum_{\omega} \bar{\xi}^{\omega} \frac{\lambda_{tr}^{\omega}}{\theta_{tr}} \tag{I-4}$$

where, λ_{tr}^{ω} is the transformation latent heat at the transformation temperature θ_{tr}.

The evolution of the plastic deformation gradient was provided by the effective plastic velocity gradient ($\tilde{L}_{pl}$), which is determined in the second intermediate configuration ($\tilde{b}$). Allowing for plastic slip in each of the constituents, the plastic velocity gradient is written

$$\begin{aligned} \tilde{L}_{pl} &= \dot{F}_{pl}\ F_{pl}^{-1} \\ &= \sum_{\beta} \tilde{\xi}^{\beta} \ \sum_{s}^{N_{sl}} \dot{\tilde{\gamma}}_{sl}^{\beta,s}\ \tilde{S}_{sl}^{\beta,s} \end{aligned} \quad . \tag{I-5}$$

In Eq. (I-5), N_{sl} is the number of slip systems, $\dot{\tilde{\gamma}}_{sl}^{\beta,s}$ is the plastic slip rate in the β phase on the s slip system. Also, $\tilde{S}_{sl}^{\beta,s} = \tilde{s}^{\beta,s} \otimes \tilde{n}^{\beta,s}$ are tensors, which are provided in terms of the normal ($\tilde{n}$) and shear ($\tilde{s}$) directions due to slip (sl). Equation (I-5) is written in the second intermediate configuration ($\tilde{b}$), where the tensors that describes slip are assumed to be predefined. The volume fractions in the reference and second intermediate configurations are related through the deformation gradients due to transformation and plasticity (i.e., $\bar{\xi}^{\phi} = J_{pl} J_{tr}\ \tilde{\xi}^{\phi} = J_{tr}\ \tilde{\xi}^{\phi}$, where $J_{pl} = 1$). The plastic entropy density rate [Tjahjanto, et. al. (2008)] reflects an average of the plastic entropy rates for each of the phases, which is analogous to the plastic velocity gradient. Similar to the plastic velocity gradient the entropy rate was written

$$\dot{\bar{\eta}}_{pl} = \sum_{\beta} \bar{\xi}^{\beta} \sum_{s} \dot{\tilde{\gamma}}_{sl}^{\beta,s} \phi_{sl}^{\beta,s} \quad . \tag{I-6}$$

In Eq. (I-6) $\phi_{sl}^{\beta,s}$ is a measure of the entropy related to plastic slip in each of the slip (sl) systems for the parent (α) and product (ω) constituents. Again, Eq. (I-6) has been expressed in terms of the slip rate ($\dot{\tilde{\gamma}}_{sl}^{\beta,b}$), which is written in the second intermediate configuration ($\dot{\bar{\gamma}}^{\beta,b} = J_{tr}\ J_{pl}\ \dot{\tilde{\gamma}}^{\beta,b}$, *where* $J_{pl} = 1$). Eqs. (I-5) and (I-6) represents an extension of the original development [Tjahjanto, et. al. (2008)] where plastic slip in only the austenitic phase was considered.

To obtain the relations, which describe the deformation of a material point that is experiencing phase transformations and plastic slip, the driving forces and the corresponding thermodynamic fluxes must be determined. For this purpose, the principles of irreversible thermodynamics were invoked [Turteltaub, et. al. (2006)]. The balance laws for energy and the rate of entropy production may be combined to provide an expression for the dissipation ($\bar{\Phi}$) in the reference configuration ($\bar{b}$)

$$\bar{\Phi} = P : \dot{F}^{T} - \bar{\rho}\left(\dot{\bar{\varepsilon}} - \theta\dot{\bar{\eta}}\right) - \bar{q}\frac{\nabla\theta}{\theta} \geq 0 \quad . \tag{I-7}$$

In Eq. (I-7), $\overline{\varepsilon}, \theta, \overline{\eta}, P, F, \overline{\rho},$ *and* $\overline{q}$ are the internal energy density, temperature, entropy density, first Piola-Kirchhoff stress, deformation gradient, density, and heat flux. For high-rate problems, the heat flux may be neglected. The internal energy density ($\overline{\varepsilon}$) in the reference configuration ($\overline{b}$) is written $\overline{\varepsilon}\left(F_{el}, \overline{\eta}_{el}, \overline{\xi}^{\phi}, \overline{\beta}_{sl}\right)$. That is, the internal energy density is written in terms of the elastic deformation gradient (F_{el}), the reversible entropy density ($\overline{\eta}_{el}$), the volume fractions of the phases ($\overline{\xi}^{\phi}$), and micro-strains due to slip ($\overline{\beta}_{sl}$). Details related to the slip micro-variables are not pursued in this development. The micro-variable for plastic slip may be found in the literature [Tjahjanto et al. (2008a); Tjahjanto et al. (2008b)].

Inserting the appropriate derivatives of the internal energy ($\dot{\overline{\varepsilon}}$), the expressions for the entropy rates ($\dot{\overline{\eta}}$), plastic deformation gradient ($\dot{F}_{pl}$), and the transformation deformation gradient ($\dot{F}_{tr}^{T}$), an expression for the dissipation may be obtained, which provides the driving forces for the fluxes of plastic slip ($\dot{\gamma}_{sl}^{\phi,\Gamma}$) and phase transformations ($\dot{\xi}^{\phi}$) in the reference configuration. For mechanics applications, it is convenient to work in the second intermediate configuration ($\tilde{b}$). Also, a conversion from internal energy to the Helmholtz free energy was made [Tjahjanto, et. al. (2008)]. A strain measure was used in place of the elastic deformation gradient. For this purpose, the Green-Lagrange strain [$\tilde{E}_{el} = \frac{1}{2}\left(F_{el}^{T} F_{el} - I\right)$], which is the energy conjugate to the second Piola-Kirchhoff stress ($\tilde{S}$), is used. Both the Green-Lagrange strain and the second Piola-Kirchhoff are defined in the second intermediate configuration. The resulting expression for the dissipation potential ($\tilde{\Phi}$) provides the constitutive model [$\tilde{S} = \left(\partial\tilde{\psi} / \partial\tilde{E}_{el}\right)$] and the reversible component of the entropy density [$\tilde{\eta}_{el} = -\left(\partial\tilde{\psi} / \partial\theta\right)$] as well as the driving force due to slip ($\tilde{\Phi}_{sl}^{\beta,s}$) and phase transformations ($\tilde{\Phi}_{tr}^{\omega}$)

$$\tilde{\Phi}_{sl}^{\beta,s} = J_{tr}\left[F_{el}\,\tilde{S}\,\tilde{S}_{sl}^{\beta,s} F_{el}^{T} + \tilde{\rho}\left(\theta\,\tilde{\phi}_{sl}^{\beta,s} - \tilde{w}_{sl}^{\beta,s}\frac{\partial\tilde{\psi}}{\partial\beta_{sl}}\right)\right] \quad , \tag{I-8}$$

$$\tilde{\Phi}_{tr}^{\omega} = J_{tr}\left[F_{el}\tilde{S}F_{tr}^{-T}\left(T_{tr}^{\omega}\right)^{T} F_{el}^{T} + \tilde{\rho}\left(\theta\frac{\lambda_{T}^{\omega}}{\theta_{T}} - \frac{\partial\tilde{\psi}}{\partial\tilde{\xi}^{\omega}}\right)\right] \quad . \tag{I-9}$$

The first term in Eq. (I-8), which is the resolved shear stress, is the dominant term in the driving force for plastic slip [Tjahjanto et al. (2008)]. The driving forces may be determined once the free energy has been prescribed. Similar to the approaches that are used in shock physics investigations [Greeff et al (2001)], a free energy will be provided for each of the constituents (ψ^{ϕ}). The average free energy is then a mass fraction ($\varsigma^{\phi} = v\,\xi^{\phi} / v^{\phi}$) weighted sum of the free energies of the constituents ($\psi = \sum_{\phi}\varsigma^{\phi}\psi^{\phi}$). A mixing term is not included in the expression for the average free energy. The forcing function ($\tilde{\Phi}_{tr}^{\omega}$), which is provided by Eq. (I-9), was used to drive the kinetics equation for the transformation ($\dot{\xi}^{\phi}$) [Turteltaub and Suiker (2006)]. As provided by Eq. (I-9), the driving force includes the

effects of shear. That is, the driving force for transformations has been written in terms of the stress tensor of the constituent ($\tilde{S}$) and not simply the volumetric component of the stress (e.g., the pressure). It may be shown [Turteltaub and Suiker (2006)] that the driving force provided by Eq. (I-9) can be related to a Gibbs' free energy [$g^{\phi} = \psi^{\phi} - v^{\phi} S^{\phi} : E_{el}^{\phi}$], which also has been defined as a driving force in the study of phase transformations. In the below constitutive model, a Helmholtz free energy, which provides the nonlinear elastic (equation of state) contribution that is a function of the specific volume in the current configuration will be used. Also, the Gibbs free energy, which is a function of pressure and temperature, will be used as the driving force for phase transformations. That is, the effect of shear on the transformation process will be neglected.

In an effort to quantify the physics of high-rate deformations of single crystals, a thermo-mechanical single-crystal model is provided. The deformation of low-symmetry materials, including the coupled effects of material anisotropy, linear or nonlinear elasticity, phase transformations, as well as plastic slip and twinning are considered. Insight into the deformation mechanics of single-crystals that are subjected to high-rate conditions is necessary for the purpose of quantifying material physics at the meso-scale (~10 μm). Modeling low-symmetry crystals presents additional complexity compared to cubic structures. Tensile-compressive anisotropy also is prevalent in low-symmetry crystals. The deformation of low-symmetry crystals results in anisotropic elastic and inelastic responses. Only diffusionless transformations are modeled. That is, only displacive transformations that are the result of a small rearrangement of the crystal lattice are considered. Nucleation events are not modeled. The theory assumes that all components within a computational element have the same deformation gradient and temperature. It is intended to use the model to explore the coupled physics related to high-rate and high-pressure deformation scenarios. Phase transformations can induce inelastic deformations in neighboring phases or the surrounding material. Only recently, has it become possible to experimentally explore the *in situ* response of shocked materials, which are undergoing the coupled effects of phase transformations and inelastic behavior. Consequently, thermo-mechanical models and numerical simulations are important for exploring, interpreting, and understanding the response of the high-rate deformations of materials. To achieve this goal, the above crystal plasticity model [Tjahjanto, et. al. (2008a), Tjahjanto, et. al. (2008b)] will be modified. A rate-dependent plasticity model is considered, which allows for material anisotropy. Titanium (Ti) was chosen as a model material in this study also because of the information (e.g. atomistic potentials and limited high-rate experimental data) that was available. Phase transformations in Ti exhibit deformation characteristics such as hysteresis, retained high-pressure phase, shear effects, and twinning, which are currently not included in many computational models. For the α to ω transformations in titanium (Ti), each material element is modeled to include the hexagonal close-packed (hcp) parent (α) phase and three variants [Jaworski, et, al. (2005)] of the hexagonal (hex) daughter phase ($\omega_1, \omega_2, \omega_3$). It is felt that the insight that may be gained through the development of a single-crystal model is necessary for the development of macro-mechanical (polycrystal) descriptions. The relative contributions from multiple and distinct deformation mechanisms will be distilled in this investigation. It also is envisioned that this model offers the opportunity to explore the deformation characteristics of energetic materials [Clayton, et. al. (2012)].

In this approach, the details of the microstructure (<1 μm) or sub crystalline deformation are not resolved. Instead, components of the inelastic deformation are modeled in a volume-averaged manner. That is, a suitable representative volume is chosen

and the sub grain details associated with slip, twinning, and transformations are modeled in an averaged sense. The single-crystal model does not resolve phase transformed or twin domains. Instead, mass or volume fractions of the transformed or twinned regions are evolved as the deformation progresses. Each constituent is allowed to possess distinct material properties. Nonlinear elasticity (i.e. and equation of state) has been included using free energies for both the α- and ω-phases. Plastic slip is modeled using a thermal activation model. An efficient pseudo-slip approach for twinning has been adopted. Both slip and twin systems are defined in an intermediate configuration in a predefined manner. It is anticipated that the model will provide insights into the impact that these relevant coupled nonlinear effects have on the high-rate deformations of single-crystals.

Because information regarding aspects of the high-rate deformation of Ti are lacking, molecular dynamics (MD) simulations were conducted in this investigation. The MD analyses provided insight into issues relate to the transformation process as well as the response of the high-pressure phase to deformations. An experimental component also was included in this investigation. In an effort to pursue the high-rate deformation above the transformation pressure, a plate impact experiment was conducted on a multi-crystal sample of Ti. The particle velocities at the back surface for three orientations of the Ti crystal with respect to the impact direction were measured. Simulations using the single-crystal model were compared with these data.

In the formulation the juxtaposition of symbols implies the summation over one set of adjacent indices (i.e., $C = A\,B = A_{km}B_{ml} = C_{kl}$). The symbol I is used to represent the second order identity tensor. The superscripts T, -1, and -T represent the transpose, inverse, and the transpose of an inverse of a second order tensor. In general, upper case symbols are second order tensors and lower case symbols are either vectors or scalors. The Greek superscripts α, β, or ω refer to material phases, r or s to slip systems, and a or b to twin systems.

The constitutive approach, which is used in this study, is provided in Sec. II. The model has its basis in the consistent thermo-mechanical framework for single crystals [Tjahjanto, et. al. (2008a), Tjahjanto, et. al. (2008b)]. Molecular dynamics (MD) simulations, which provide the high-rate deformation characteristics of single-crystal Ti, are provided in Sec. III. A description of the plate impact experiment for a multi-crystal sample of Ti and resulting particle velocity data are discussed in Sec. IV. In Sec. V, simulations using the proposed model are compared to the data obtained from the single-crystal Ti experiment. Finally, summary remarks and future considerations will be addressed in Sec. VI.

II. Constitutive Model

In an effort to address the high-strain-rate deformation of hcp materials, the framework that was reviewed in Sec. I [Tjahjanto, et. al. (2008a), Tjahjanto, et. al. (2008b)] is generalized in a heuristic fashion. The extension includes free energies, from which nonlinear elasticity (equation of state) and the driving force for the phase transformations are incorporated. Plasitic slip is included in each of the constituents. Also, a pseudo-slip approach is used to include twinning in the parent (α) phase. The model is based on the multiplicative decomposition [Eq. (I-1)] of the deformation gradient [Tjahjanto et al. (2008a), Tjahjanto et al. (2008b)]. Once constitutive models are provided for the plastic and transformation deformation gradients, the elastic deformation gradient and the elastic

strains ($\tilde{E}_{el}$) may be determined. Models for plastic slip and twinning are provided. It is assumed that the plastic deformation is isochoric [$J_{pl} = \det(F_{pl}) = 0$].

The transformation component of the deformation gradient is provided by Eq. (I-3) [Turteltaub and Suiker (2006)]. Values for the shape strain vector and the habit plane normal are obtained from molecular dynamics simulations (Sec. III). For the transformation from the low-pressure (α) phase to the high-pressure (ω) phase in Ti, the Silcock mechanism is used (Sec. III). That is, the model will include the α–phase and three variants of the ω–phase ($\omega = 1,2,3$). It may be shown that [Turteltaub and Suiker (2006)]

$$J_{tr} = \det(F_{tr}) = \tilde{v} / v_0 \approx 1 + \delta_{tr} \sum_{\omega} \xi^{\omega} \qquad \text{(II-1)}$$

where, $\tilde{v}$ and v_0 are the specific volumes in the intermediate and reference configurations. Similarly,

$$J_{tr}^{\phi} = \det(F_{tr}^{\phi}) = \tilde{v}^{\phi} / v_0 = 1 + \delta_{tr} \qquad . \qquad \text{(II-2)}$$

In Eq. (II-2), $J_{tr}^{\phi=\alpha} = 1$ and δ_{tr} is the volume change due to the transformation. It is assumed that the volume change is the same for each of the ω-variants. For Ti, there is approximately a 1.6% volume reduction due to the transformation. Consequently, the deformation gradient (F_{tr}) may be obtained once the volume fraction (ξ^{ω}) for each of the ω variants has been obtained. An equation for the transformation kinetics is used to determine ξ^{ω}.

The plastic component of the deformation gradient (F_{pl}) is obtained from a constitutive model for plastic velocity gradient ($\tilde{L}_{pl} = \dot{F}_{pl} F_{pl}^{-1}$). In the model, the plastic velocity gradient [Eq. (I-5)] allows for plastic slip in the α-phase and the ω-variants and twinning [Salem et al. (2005); Kalidindi (1998)] only in the α-phase. The plastic velocity gradient in the intermediate configuration is written

$$\tilde{L}_{pl} = \varsigma^{\alpha} \left\{ \left(1 - \sum_{a} \tilde{f}^{a} \right) \sum_{s} \dot{\tilde{\gamma}}_{sl}^{\alpha,s} \tilde{S}_{sl}^{\alpha,s} + \sum_{a} \dot{\tilde{f}}^{a} \tilde{\gamma}_{tw} \tilde{S}_{tw}^{a} \right\} + \sum_{\omega} \varsigma^{\omega} \sum_{s} \dot{\tilde{\gamma}}_{sl}^{\omega,s} \tilde{S}_{sl}^{\omega,s} \, . \qquad \text{(II-3)}$$

In Eq. (II-3), $\dot{\tilde{\gamma}}_{sl}^{\alpha,s}$ is the plastic strain rate in the α-phase on the s[th] slip system, $\tilde{\gamma}_{tw}$ is the constant shear strain associated with twinning, $\tilde{f}^{a}$ is the volume fraction of twins in the α-phase on the a[th] twin system, and $\tilde{S}^{a} = \tilde{s}^{a} \otimes \tilde{n}^{a}$ is the tensorial direction of the shear resulting from active slip ($S_{sl}^{\alpha,s}$) or twin (S_{tw}^{α}) systems, where $\tilde{s}^{a}$ and $\tilde{n}^{a}$ are unit vectors along and normal to the slip or twin directions. Therefore, the plastic velocity gradient may be obtained once constitutive models have been provided for the plastic shear rate ($\dot{\tilde{\gamma}}_{sl}^{\alpha,s}$) and the rate of increase of the twin volume fraction ($\dot{\tilde{f}}^{a}$), which are derived in terms of the appropriate driving forces.

The evolution of plastic slip is modeled using a phenomenological hardening law. The plasticity model is appropriate for thermally activated dislocation motion. That is, the

effects of dislocation drag are neglected. The thermal activation model, which has been used to calculate the shearing rate due to slip [Bronkhorst et al. (2007)], is written as a function of the resolved shear stress ($\tau^{\alpha,s}$) on the sth-slip system of the α -phase.

$$\dot{\gamma}^{\alpha,s} = \dot{\gamma}_0 \, \mathrm{sgn}(\tau^{\alpha,s}) \exp\left\{ -\frac{E_0}{k_B \theta} \left\langle 1 - \left\langle \frac{\left|\tau^{\alpha,s}\right| - g^{\alpha,s}}{g_l^{\alpha,s}} \right\rangle^{p} \right\rangle^{q} \right\} \qquad \text{(II-4)}$$

where

$$\begin{aligned} \dot{g}^{\alpha,s} &= g_{sl} \sum_r \left(\frac{g_s^{\alpha,r} - g^{\alpha,r}}{g_s^{\alpha,r} - g_0^{\alpha,r}} \right) \left[\breve{r} + (1 - \breve{r}) \delta^{\alpha r} \right] \left| \dot{\gamma}^{r} \right| \\ g_s^{\alpha,s} &= g_{s0}^{\alpha,s} \left| \frac{\dot{\gamma}^{\alpha,s}}{\dot{\gamma}_0} \right|^{k\theta/A} + g_{hp}^{\alpha,s} \left(\sum_b f^b \right)^{1/2} \end{aligned} \qquad \text{(II-5)}$$

In Eq. (II-4), $\langle x \rangle = \frac{1}{2}\left(x + |x| \right)$ is the Macaulay bracket. Also, $g^{\alpha,s}$ is the slip system resistance of the α phase on the s slip system. The hardening model includes both self-hardening and cross-hardening through the use of the self-hardening ratio ($\breve{r}$). The material parameter $g_{hp}^{\alpha,s}$ accounts for the Hall-Petch effect [Salem et al. (2005)] that results from the effective reduction in grain size due to twinning, g_{sl} provides the initial hardening rate, and $g_{s0}^{\alpha,s}$ is the saturation value at 0 K in the absence of twinning. Also, $g_s^{\vartheta,\alpha}$ is the saturation stress, $g_0^{\vartheta,\alpha}$ is the initial slip system resistance, k_B is the Boltzman constant, and E_0 is the activation energy. The exponents p and q control the dislocation spatial energy barrier profile. The resolved shear stress is assumed to be the dominant term in the driving force for plastic slip [Eq. (I-8)]. Also, the effect of elastic stretch on the calculation of the resolved shear stress is neglected [Kalidindi et al. (1992)]. Therefore the resolved shear stress [Eq. I-8)] is written as

$$\tau^{\alpha,s} \approx \tilde{S} : \tilde{S}^{\alpha,s} = \tilde{S} : \left(\tilde{s}^{\alpha,s} \otimes \tilde{n}^{\alpha,s} \right)_{sym} \quad . \qquad \text{(II-6)}$$

Titanium is a highly anisotropic material. Furthermore, a realistic model, which addresses the important deformation modes of Ti should include twinning. Twinning is modeled using a pseudo-slip [Salem et al. (2005); Kalidindi (1998)] approach. Twinning is considered only in the α-phase [Eq. (II-4)]. It is assumed that the twinned and untwined (matrix) regions experience the same deformation gradient. Both slip and twinning are prohibited in twinned regions. The lattice orientations that are produced at different instances of the deformation path are assumed to be identical for the same twin system. Account of the differences in the lattice orientations of the twinned regions is included by rotating the stiffness tensor ($\mathbb{C}^a$) of the matrix into the orientation of the twinned region ($\mathbb{C}^\alpha$)

$$\mathbb{C}^a = Q : Q : Q : Q : \mathbb{C}^\alpha \qquad \text{(II-7)}$$

where Q is the transformation matrix between the lattice orientation in the matrix to the lattice orientation in the twinned region

$$Q=2n\otimes n-I \tag{II-8}$$

and n is the normal to the twin plane [Kalidindi (1998)]. A power law model [Salem et al. (2005)] is used to describe the evolution of the deformation twin volume fractions

$$f^a=\frac{\dot{\gamma}_{tw0}}{\gamma_{tw}}\left(\frac{\left|\tau^a\right|}{h^a}\right)^{a_{tw}}. \tag{II-9}$$

In Eq. (II-9), $\dot{\gamma}_{tw0}$ is the reference twinning rate and γ_{tw} is the twinning strain. In the current implementation, the twin volume fraction must remain positive ($f^a\geq 0$) and the sum of the volume fractions of all of the twin orientations is bounded ($\sum_a f^a\leq 1$). When twinning is included in the plastic velocity gradient ($\tilde{L}_{pl}$), then a driving force similar to that obtained for slip [Eq.(I-8)] may be obtained as the driving force for the production of twins ($\hat{\dot{f}}^{\omega,a}$). Again, the dominant term in the driving force for twinning is assumed to be the resolved shear stress on the a-twin system ($\tau^{\alpha,a}=\tilde{S}:S^{\alpha,a}=\tilde{S}:\left(\tilde{m}^{\alpha,a}\otimes\tilde{n}^{\alpha,a}\right)_{sym}$). The twin hardening function is written [Salem et al. (2005)]

$$\dot{h}^a=h_{tw}\left(\sum_b\gamma_{tw}\dot{f}^b\right)\left(\sum_c\dot{f}^c\right)^{b_{tw}}+h_{sl}\left(\sum_p\dot{\gamma}_{sl}^{\alpha,p}\right)\left(\sum_q\gamma_{sl}^{\alpha,q}\right)^{d_{tw}}. \tag{II-10}$$

The first term on the right of Eq. (II-10) accounts for hardening due to twin-twin interactions and the second term represents hardening due to slip-twin interactions. In Eqs. (II-9) and (II-10), h_{tw}, h_{sl}, a_{tw}, b_{tw}, and d_{tw} are material parameters.

The formulation of a constitutive model requires work conjugate measures for the stress and strain. The ability to address shock propagation effects is facilitated by including nonlinear elasticity or an equation of state. The incorporation of an equation of state requires the implementation of a pressure-volume relation. Therefore, it is necessary to decompose the strain into volumetric and isochoric components. For this reason, an elastic strain is employed, which results in a traceless strain measure for an isochoric deformation. An isochoric deformation does not result in a contribution to the pressure for an isotropic material or a crystal with cubic symmetry. Many models for high-rate applications use the logarithmic strain and Kirchhoff stress, which are defined in the unrotated configuration [Becker (2004)] between the second intermediate and current configurations. In this model, the second Piola-Kirchhoff stress ($\tilde{S}$) and the elastic Green-Lagrange strain [$\tilde{E}_{el}=\frac{1}{2}\left(F_{el}^TF_{el}-I\right)$], which are defined in the second intermediate configuration, are used. The elastic deformation gradient ($F_{el}=F_{ed}F_{ev}$) is decomposed into an isochoric ($F_{ed}=J_{el}^{-1/3}F_{el}$) and volumetric ($F_{ev}=J_{el}^{1/3}I$) component. This results in a volumetric ($\tilde{E}_{ev}$)

and isochoric ($\tilde{E}_{ed}$) component of the Green-Lagrange strain ($\tilde{E}_{el}$) [Bonet and Wood (1997), Luscher et al. (2016)]. The resulting strain measures are

$$\tilde{E}_{el} = \frac{1}{2}(F_{el}^T F_{el} - I) = \tilde{E}_{ed} + \tilde{E}_{ev} = \tilde{E}_{ed} + \tilde{e}_{ev} I \qquad \text{(II-11)}$$

where

$$\begin{aligned} \tilde{E}_{ev} &= \frac{1}{2}(J_{el}^{2/3} - 1)\, I \\ \tilde{E}_{ed} &= \frac{1}{2}(F_{el}^T F_{el} - J_{el}^{2/3} I) \end{aligned} \quad . \qquad \text{(II-12)}$$

Therefore, the elastic strains are obtained once the elastic deformation gradient ($F_{el} = F\, F_{tr}^{-1}\, F_{pl}^{-1}$) has been determined from the total, transformation, and plastic deformation gradients.

The constitutive model may be obtained from the definition of the Helmholtz free energy. Classical approaches for low-strain rate deformations consider a linear, thermo-elastic expression for the Helmholtz free energy ($\tilde{\psi}$). Excluding contributions due to interfaces or defects [Tjahjanto et al. (2008)] a classical free energy may be written

$$\tilde{\psi}(\tilde{E}_{el}, \theta) = \frac{1}{2}\, \tilde{E}_{el} : \tilde{\mathbb{C}} : \tilde{E}_{el} - \frac{c_v}{2\,\theta_{ref}}\left(\theta - \theta_{ref}\right)^2 + \tilde{\rho}\eta_{ref}\left(\theta - \theta_{ref}\right) + \tilde{\rho}\psi_{ref} \,. \qquad \text{(II-13)}$$

In Eq. (II-13), $\tilde{\mathbb{C}}$ is the fourth order elastic stiffness tensor, c_v the heat capacity at constant volume, $\tilde{\rho}$ the density, and $\tilde{\eta}$ the entropy. Eq. (II-13) then may be used to compute the stress [$\tilde{S} = \left(\partial\tilde{\psi} / \partial\tilde{E}_e\right)_\theta$] and the entropy [$\tilde{\eta} = \left(\partial\tilde{\psi} / \partial\theta\right)_{\tilde{E}_{el}}$]. Therefore, allowing for a pressure and temperature dependent stiffness ($\tilde{\mathbb{C}}$)

$$\tilde{S} = \tilde{\mathbb{C}} : \tilde{E}_{el} + \frac{1}{2}\left[\, \tilde{E}_{el} : \frac{\partial\tilde{\mathbb{C}}}{\partial\tilde{p}} : \tilde{E}_{el} \right] \frac{\partial\tilde{p}}{\partial\tilde{e}_{ev}}\, I \quad . \qquad \text{(II-14)}$$

The pressure derivative ($\partial\tilde{p} / \partial\tilde{e}_{ev}$) multiplying the last term in Eq. (II-14) is the negative of the bulk modulus. Expressing Eq. (II-14) in terms of volumetric ($\tilde{S}_v, \tilde{E}_{ev}$) and deviatoric ($\tilde{S}_d, \tilde{E}_{ed}$) components [Luscher et al. (2016); De et al. (2014); Becker (2004)] provides

$$\begin{aligned} \tilde{S}_d &= L_d : \tilde{\mathbb{C}} : \tilde{E}_{ed} \\ \tilde{s}_v &= \left\{ \frac{1}{9}\left[I : \tilde{\mathbb{C}} : I \right] \tilde{e}_{ev} + \frac{1}{18}\left[I : \frac{\partial\tilde{\mathbb{C}}}{\partial\tilde{p}} : I \right] \left(\tilde{e}_{ev}\right)^2 \frac{\partial\tilde{p}}{\partial\tilde{e}_{ev}} \right\} + \frac{1}{3}\left[\tilde{E}_{ed} : \tilde{\mathbb{C}} : I \right] \quad . \qquad \text{(II-15)} \\ &\quad + \left\{ \frac{1}{2}\left[\tilde{E}_{ed} : \tilde{\mathbb{C}} : \tilde{E}_{ed} \right] + \frac{1}{9}\left[\tilde{E}_{ed} : \frac{\partial\tilde{\mathbb{C}}}{\partial\tilde{p}} : \tilde{e}_{ev} I \right] \right\} \frac{\partial\tilde{p}}{\partial\tilde{e}_{ev}} \end{aligned}$$

In Eq. (II-15), L_d is a fourth order operator that extracts the deviatoric component from a second order tensor [Becker (2004)]. It should be observed that for low-symmetry crystals, the volumetric and deviatoric components of the stress and strain are coupled. For high-rate applications, a linear dependence of the stress on the strain will not address shock propagation scenarios. A nonlinear elastic formulation is necessary to facilitate the steepening of the propagating wave-front for shock conditions. Consequently, the first term in brackets of the second equation in Eq. (II-15), which relates the volumetric component of stress to the volumetric component of strain, is replace by an expression for nonlinear elasticity, or an equation of state [Luscher et al. (2016); De et al. (2014)]

$$\tilde{s}_{eos} \equiv \left\{ \frac{1}{9}\left[I : \tilde{\mathbb{C}} : I \right] \tilde{e}_{ev} + \frac{1}{18}\left[I : \frac{\partial \tilde{\mathbb{C}}}{\partial \tilde{p}} : I \right] \left(\tilde{e}_{ev} \right)^2 \frac{\partial \tilde{p}}{\partial \tilde{e}_{ev}} \right\} \Rightarrow \tilde{p}_{eos} \quad . \tag{II-16}$$

The equation of state [$p_{eos}(v,\theta) = -\partial \psi_{eos}(v,\theta)/\partial v$] is obtained from a free energy. It should be noted that the constitutive model [Eq. (II-15)] is written for each of the constituents using the assumption of uniform elastic strain and temperature. Unique properties are used to determine the stresses [$\tilde{S}^{\phi} = \tilde{S}^{\phi}(\tilde{E}_{el}, \theta);\ \phi = \alpha, \omega$] for each phase, variant, and twin.. The total stress at a material point is obtained as a volume average of the stresses of the constituents [Kalidindi (1998)]

$$\tilde{S} = \varsigma^{\alpha} \left\{ \left(1 - \sum_a f^a \right) \tilde{S}^{\alpha} + \sum_a f^a \tilde{S}^a \right\} + \sum_{\omega} \varsigma^{\omega}\ \tilde{S}^{\omega} \tag{II-17}$$

where ς^{α} and ς^{ω} are the volume fractions of the α-phase and the ω-variants and f^a are the volume fractions of the twinned regions in the α-phase.

The transformation deformation gradient (Eq. II-3) may be obtained once the volume fractions (ξ^{ϕ}) of each constituent have been determined from the transformation kinetics. In this approach, the driving force for the transformation is taken to be the Gibbs free energy. The transformation rate of change for the mass fraction of the ω-variant is represented by the exponential function [Greeff et al. (2002)]

$$\dot{\xi}^{\omega} = \left[1 - c_{tr} \left(\xi^{\omega} \right)^2 \right] \varpi\ \frac{\Delta g}{\beta_{tr}} \exp\left\{ \left(\frac{\Delta g}{\beta_{tr}} \right)^2 \right\} \quad . \tag{II-18}$$

The first term on the right of Eq. (II-18) places a lower bound on the production of the ω-variant and $\Delta g = g^{\alpha} - g^{\omega}$ is the change in the Gibbs free energy of the α-phase and ω-variants. Only free energies for the α- and ω-phases are available. It has been shown from atomistic simulations (Sec. III) and experiment that the transformation from α-Ti to ω–Ti includes the effects of shear as well as a volume change [Ivanisenko et al. (2008); Zong et al. (2014)]]. The ability to include the effects of shear in the transformation driving force was provided in Eq. (I-9). However, the free energies that are used in the model are compatible with a pressure versus temperature equilibrium phase diagram for Ti [Young (1976)]. Consequently, the effects of shear on the transformation process are neglected in the model. Furthermore, the change of the Gibbs free energies that are used in Eq. (II-18) are written in

terms of an average pressure ($g^k = \psi^k + p\, v^k$). The above assumptions allow only for the equal production of the three ω-variants. The lack of quantitative information for high-rate, high-pressure deformations of low-symmetry crystals has motivated this heuristic approach.

The constitutive model and the transformation kinetics are determined once a free energy has been defined. Helmholtz free energies for the nonlinear elastic component of each phase (ψ^{ϕ}_{eos}), which are based on information provided by electronic structure calculations, have been developed [Greeff (2005) and Greeff et al. (2001)]. These free energies place an emphasis on the equilibrium phase diagram [Young (1991)] and the deformation path along the shock Hugoniot. Formulations are provided in terms of the static lattice energy (ψ_0), ion motion free energy energy (ψ_{vib}), and electronic excitation energy (ψ_{el}). These free energies are provided in terms of the specific volume (v^{ϕ}) and temperature (θ) in the current configuration. Analytic expressions for the nonlinear elastic component (ψ^{ϕ}_{eos}) of the free energies of each phase [ψ^{ϕ}_{eos}, $\left(\phi = \alpha, \omega \ phases\right)$] are available for both Ti and Zr [Greeff (2005); Greeff et al. (2001)]. The Helmholtz free energy for Ti is written [Greeff (2005)]

$$\psi^{\phi}_{eos}(\tilde{\varepsilon}_{ev},\theta) \rightarrow \psi^{\phi}_{eos}(v^{\phi},\theta) = \psi^{\phi}_{0}(v^{\phi}) + \psi^{\phi}_{vib}(v^{\phi},\theta) + \psi^{\phi}_{el}(v^{\phi},\theta) \ . \qquad \text{(II-19)}$$

In Eq. (II-19), the static lattice potential [the superscript denoting the phase (ϕ) is omitted for convenience] is

$$\begin{aligned} \psi_0(v) &= \psi^* + \frac{4 v^* B^*}{\left(B_1^* - 1\right)^2}\left[1 - \left(1+\eta\right)\exp(-\eta)\right] \\ \eta &= \frac{3}{2}\left(B_1^* - 1\right)\left[\left(\frac{v}{v^*}\right)^{1/3} - 1\right] \end{aligned} \ . \qquad \text{(II-20)}$$

The high-temperature expansion has been used for the lattice vibrational free energy (ψ_{vib})

$$\begin{aligned} \psi_{vib}(v,\theta) &= 2R\theta\left\{-\ln\left[\frac{\theta}{\theta_0(v)}\right] + \frac{1}{40}\left[\frac{\theta_2(v)}{\theta}\right]^2\right\} \\ \theta_2(v) &= \theta_0(v)\, e^{1/3} \\ \theta_0(v) &= \theta_0^* \exp\left\{-\frac{\gamma_0}{v_0}\left(v - v_0\right)\right\} \end{aligned} \ . \qquad \text{(II-21)}$$

Finally, the electronic excitation free energy (ψ_{el}) is written

$$\psi_{el}(v,\theta) = -\frac{1}{2}\Gamma_0\left(\frac{v}{v_0}\right)^{\kappa}\theta^2 \ . \qquad \text{(II-22)}$$

In the above equations, B^* and B_1^* are the bulk modulus and its pressure derivative at the equilibrium volume. Also, $\psi^*, v_0, v^*, \theta_0^*, \Gamma_0, \kappa,$ and γ_0 are material parameters.

Once a (Helmholtz) free energy for each phase (ψ^ϕ) is constructed, expressions for the nonlinear elastic component of the stress ($p_{eos}^\phi = -\partial\psi_{eos}^\phi / \partial v^\phi$) and the driving forces for the phase transformation (g^ϕ) may be obtained. Also, derivatives of the free energy provide thermodynamic properties (e.g. the isothermal bulk modulus $B = v\dfrac{\partial^2\psi}{\partial v^2}$, the specific heat at constant volume $c_v = -\theta\dfrac{\partial^2\psi}{\partial\theta^2}$, the Gruneisen parameter $\Gamma = -\dfrac{v}{c_v}\dfrac{\partial^2\psi}{\partial v\partial\theta}$, as well as the thermal expansivity $\alpha = \dfrac{\Gamma\, c_v}{v\, B}$).

Finally, the temperature is updated using the second law of thermodynamics (Luscher et. al. (2016); De et al. (2015)]

$$\dot{\theta} = \theta\,\Gamma : \dot{E}_e + \frac{v}{c_v}\left(\beta_{sl}\sum_{\vartheta}\xi^{\vartheta}\sum_{\alpha}\tau^{\vartheta,\alpha}\dot{\gamma}_{sl}^{\vartheta,\alpha} + \beta_{tw}\xi^{\alpha}\sum_{a}\tau^{a}\dot{\gamma}_{tw}^{a}\right) \quad . \qquad \text{(II-23)}$$

The first term in Eq. (II-23) is the reversible work due to elastic strains, the second term is the irreversible work due to plastic slip, and the last term is the irreversible work due to twinning. The beta-factors (β_{sl} and β_{tw}) in Eq. (II-23) reflect the fact that not all of the inelastic work is converted to internal energy or temperature but that some of the energy is stored in the evolving microstructure (e.g. trapped in the lattice strain energy). In general, the beta-factors may be a function of the strain rate. In this model they will be assumed to be constant.

III. Molecular Dynamics Simulations

In an effort to explore the high-rate deformation of materials, including the effects of plastic slip, twinning, and phase transformations, titanium (Ti) was chosen as a representative material. Titanium represented a convenient material because of the wealth of knowledge that was available from both experimental and theoretical investigations. Considerations at many length scales have been pursued for this material. Initially, molecular dynamics (MD) simulations, using available atomistic potentials, were considered. Issues related to the transformation pathway, the deformation characteristics of the high-pressure (ω) phase, and single-crystal model parameters such as the shape strain tensor were considered in the MD simulations.

Molecular dynamics simulations were performed on single crystals using a potential, which is consistent with the polycrystal shock Hugoniot data from flyer plate experiments [Marsh (1980)]. The simulations were performed in a microcanonical ensemble using the LAMMPS code [Plimpton (1995)]. The interatomic interactions in Ti were described by a modified embedded atom potential [Hennig et al. (2008)], which gives accurate total

energies, elastic constants, and phonon spectra, as well as reasonable values for point defects and surface and stacking fault energies. Simulations for 0.2 μm-thick single crystal Ti samples were considered, using up to 3.0 million atoms. After isothermally annealing the sample at 30 K for 1.2 ns, the left surface of the system was driven by a piston with a particle velocity of 0.75 km/s and peak pressure 14 GPa, which is above the threshold piston velocity of 0.57 km/s that is required to induce a phase change in Ti.

It was previously shown that the transformation pathway [Zong et al. (2014)] in simulated, shocked samples of Ti obeys the experimentally observed Silcock orientation relationship (OR) between the low-pressure (hcp) α-phase and high-pressure (hex) ω-phase that is shown in Fig. 2 [Jyoti et al. (2008)]. It is this same OR, which we use in our phenomenological single-crystal model. However, we note that this transformation is accompanied by hysteresis and can be irreversible with the high-pressure ω-phase retained partially or almost fully after unloading under ambient conditions. Although this is well established under both static and shock conditions, the crystallographic nature of the transformation in Ti and Zr is still open to question as the dependence of the ORs on loading conditions is not clear. Measurements to date have been primarily on polycrystalline samples and the anisotropy in shock response as well as residual stresses are not easily inferred from these measurements. Thus, we have used simulations on single crystals to provide insight into factors mediating the phase transformation process.

The loading of an ideal hcp Ti crystal under shear at a strain rate of 10^8/s and the complexity of the process is illustrated in Fig. 3. As the crystal is sheared, it first is deformed elastically and at some relatively large strain, it yields with a drop in the stress and nucleates the characteristic stacking of the ω-phase. On further loading, the α-phase largely transforms to the ω-phase. The OR on this forward transformation phase is the familiar Silcock OR or transformation pathway. On further shearing, the ω-phase reverts back to α-phase. There is a lower barrier to the reverse transformation than to dislocation nucleation and plastic deformation of the ω−phase. Moreover, this reverse transformation does not follow the same OR as the Silcock mechanism because the initial state is quite different from the forward transformation. The habit plane between the α- and ω-phases for the forward transformation in a single crystal is shown in Fig. 4. The terracing emphasizes the dislocation-mediated origin of the inhomogeneous shear. The habit plane normal (m^{ω}) and shape strain vector (b^{ω}) are obtained from these simulations [Eq. (I-3)].

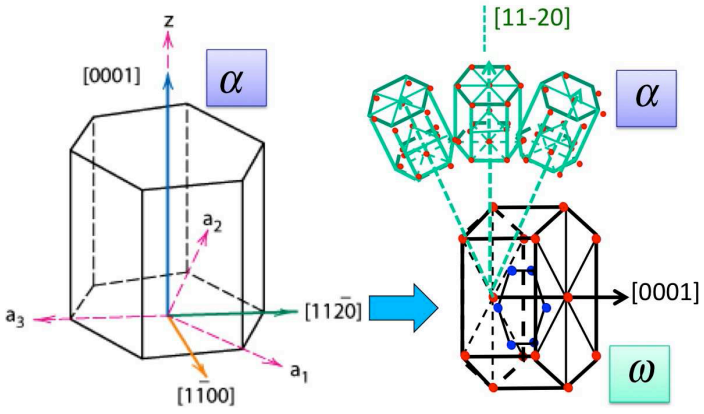

Fig. 2. The Silcock orientation relationship (OR), which arises in the MD simuiations from coexisting α- and ω-phases. This OR is used in the phenomenological single-crystal model.

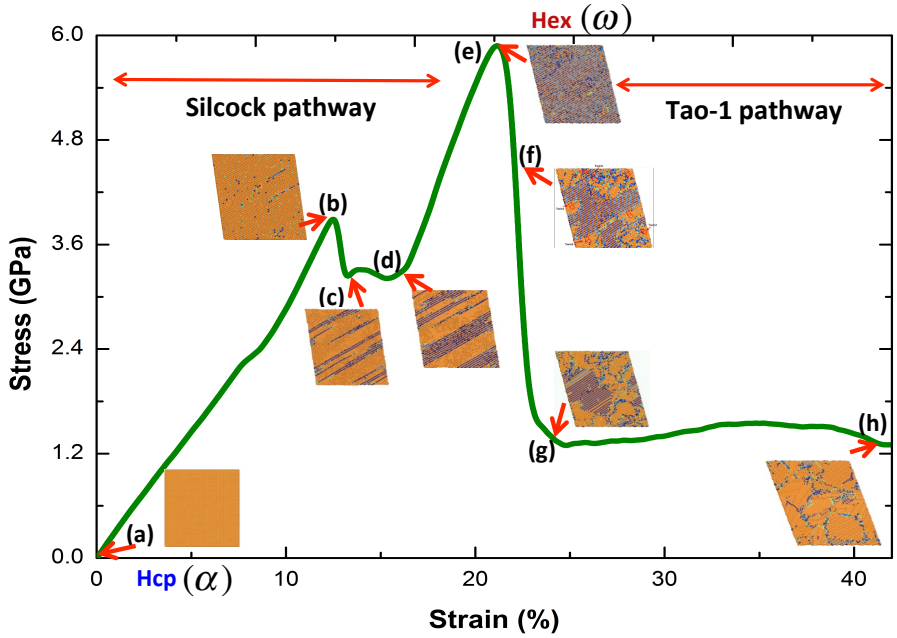

Fig. 3: The dependence of the transformation mechanism and pathway on the loading coditions and the residual strains. The pristine α-phase undergoes the Silcock OR on shearing with nucleating and growth of the ω-phase. Further shearing of the transformed ω-crystal results in the reverse transformation to the α-phase rather than plastic deformation of the ω-phase.

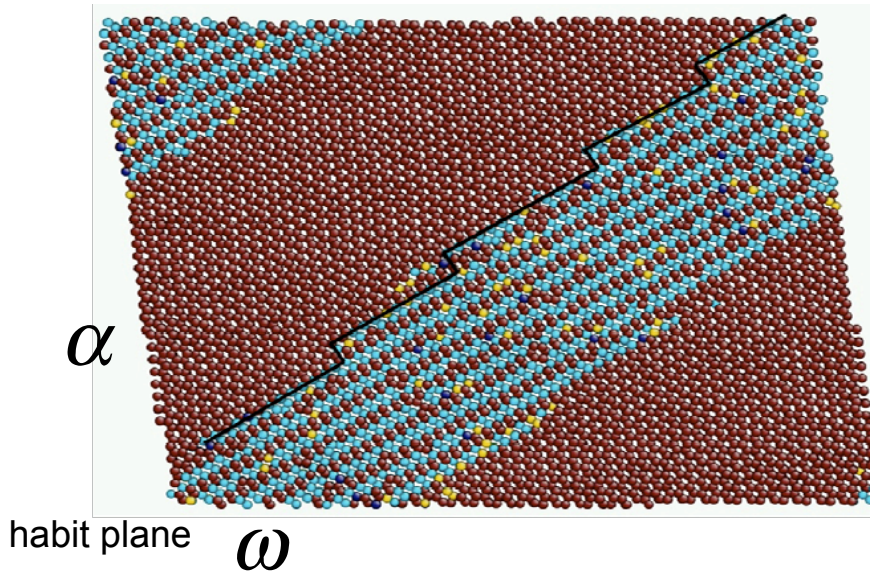

Fig. 4: The habit plane between the a- and w-phases, showing that the homogeneous shear results from dislocation-mediated plasticity.

IV. Multi-Crystal Experiment

A multi-crystal, plate-impact experiment was conducted, in an effort to explore the high-rate response of single crystals of titanium (Ti). A high-purity (99.99%) Ti multi-crystal, composed of large grains, which extended completely through the thickness of the sample, was impacted with a polycrystalline OFHC copper flyer. A micrograph of the multi-crystal Ti sample is provided in Fig. 5. The thickness of the flyer and the sample were 2.032 mm and 1.502 mm, respectively. The diameter of the flyer was 38 mm. The 10.06 mm diameter Ti sample was embedded in a Ti momentum trap. A schematic diagram of the experiment is provided in Fig. 6. The velocity of the projectile was 0.956 mm/μs. A peak pressure in the Ti sample was estimated as 14.5 GPa. A photon doppler velocimeter (PDV) probe was attached to three of the crystals within the target. Each grain represented a different crystal orientation relative the impact load. The impact direction was along the $[0001]$, $[10\bar{1}0]$, and $[3\bar{1}\bar{4}4]$ orientations for the three grains (Fig. 5). The PDV probes provided the history of the particle velocity at the back surface of the three grains. The crystals were sufficiently large that grain boundary and edge effects were largely avoided within the times of the free-surface velocity measurement. The measured particle velocity as a function of time provides the distinct differences between the three crystal orientations. The velocity histories of the three measurements are provided in Fig. 7. In the figure, the velocity history of the three grains has been displaced in time. The elastic precursor for the [0001] oriented grain is much higher than the $[10\bar{1}0]$ and $[3\bar{1}\bar{4}4)$ orientations. This is likely a result of the relatively large sound speed in the [0001] direction in the Ti single crystal. It may also indicate that there is a delayed activation of primary deformation due to slip or twinning mechanisms for this orientation. A sharp kink was observed in the $[10\bar{1}0]$ and $[3\bar{1}\bar{4}4]$ orientations at 0.9 mm/μs. This feature was not observed in the velocity trace of the $[0001]$ crystal orientation. This kink is generally attributed to the onset of the α- to ω-phase transformation. The pressure associated with the kink is in line with previous expectation based on similar experiments performed on polycrystalline high-purity Ti samples. It was thought that the absence of a distinct kink in the $[0001]$ orientation at 0.9 mm/μs indicated that the transition had been overdriven at this pressure. Additionally, the plastic wave in the $[0001]$ orientation exhibits a lower slope that the other orientations. The slope of the plastic portion of the curve in the $[0001]$ oriented grain may indicate that the α– to ω-transformation occurs over a relatively long period of time. Postulated locations of the elastic precursor and the transformation from the α- to the ω-phase are superimposed on the Fig. 7.

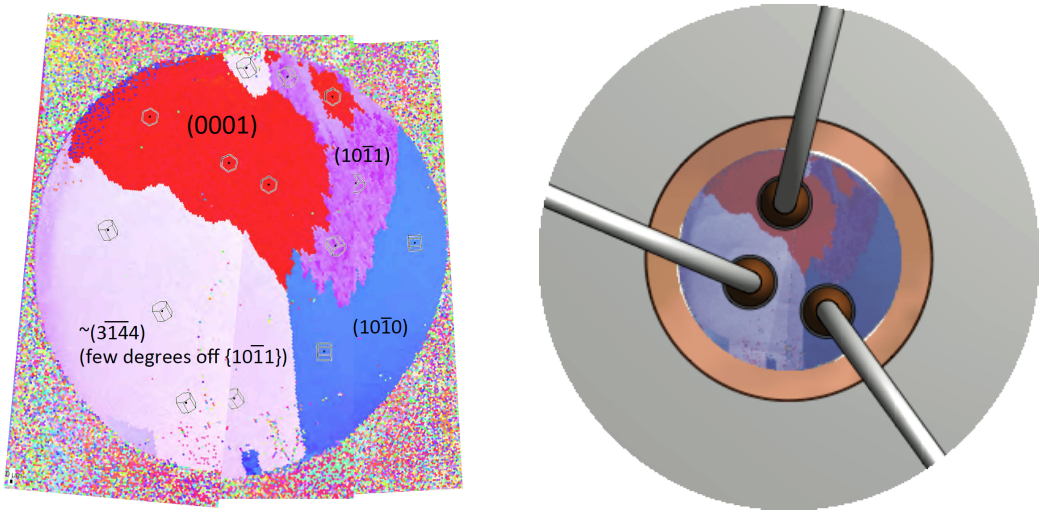

Fig. 5: Micrograph of the Ti multi-crystal sample. (a) The red region is the $[0001]$ orientation, purple the $[10\,\bar{1}1]$ orientation, blue the $[10\,\bar{1}0]$ orientation, and gray the $[3\,\bar{1}\bar{4}4]$ orientation. (b) Location of the PDV probes.

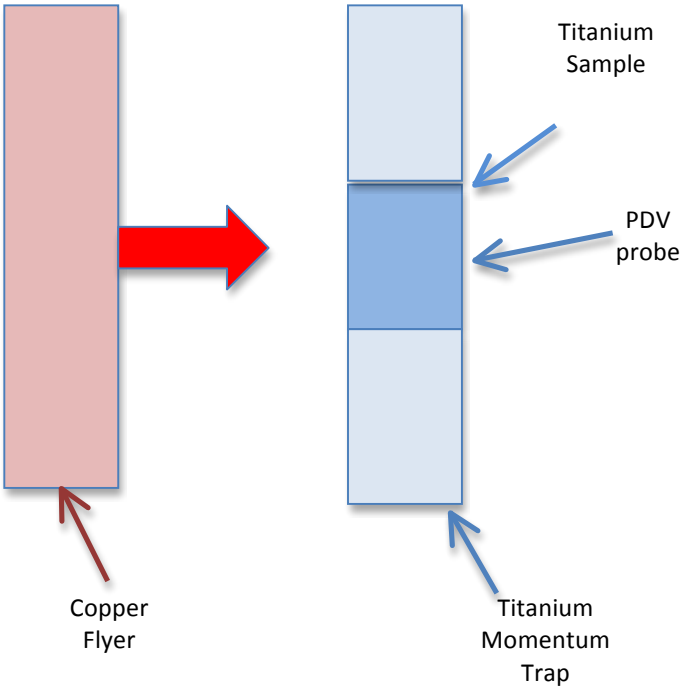

Fig. 6: Schematic of the multi-grain Ti plate-impact experiment.

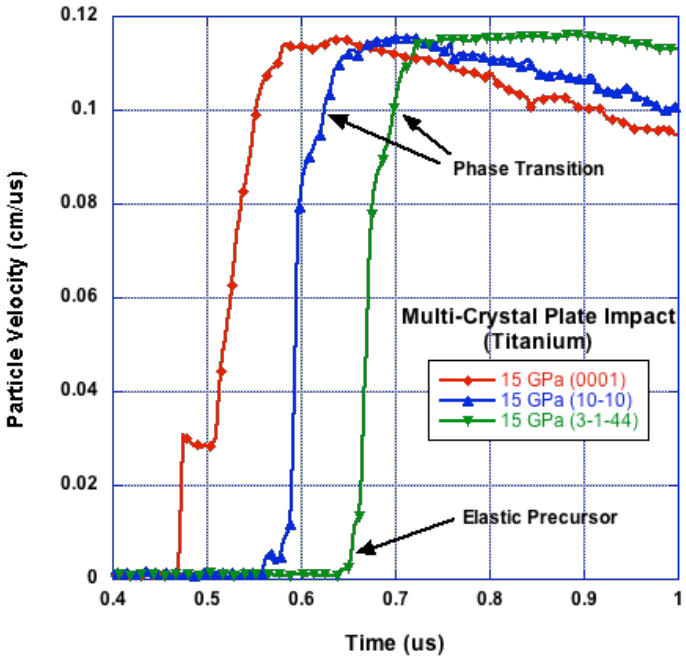

Fig. 7. Multi-crystal titanium impact experiment (a) experiment schematic, (b) multi-crystal sample showing the PDV probes, (c) measured particle velocity versus time at the back of each single-crystal for the [0001], [10-10] and [3-1-44] orientations.

V. Simulations

Computational simulations were performed in an effort to highlight the ability of the single-crystal model to capture the features of the high-rate deformation of Ti crystals. Many of the parameters for the constitutive model are not readily available for the conditions of high rates and pressures. This is especially true for the high-pressure ω-phase. Simulations of the multi-crystal experiment that was described in Sec. IV were conducted. Plate impact or uniaxial strain experiments have been valuable for investigating the deformation characteristics of materials at high-strain rates [Winey et al. (2004); Winey et al. (2006), Becker (2004)]. Particle velocities at the back of the Ti target were measured using PDV probes (Figs. 5 and 6). The model parameters that were used in the simulations are provided in Tables I through IX. Anisotropic, elastic constants for the α-phase are available in the literature [Vohr (1978); Fisher et al. (1964)]. The elastic constants that were used in the simulations for the α- and ω-phases are provided in Table I. The pressure and temperature derivatives of the stiffness tensor

$$\mathbb{C}(p,\theta) = \mathbb{C}_0 + \frac{\partial \mathbb{C}}{\partial p}\, dp + \frac{\partial \mathbb{C}}{\partial \theta}\, d\theta \approx \mathbb{C}_0 \qquad \text{(V-1)}$$

were not included in the analyses. The parameters that were used for the equation of state are provided in Table II [Greeff et al. (2001)] for both the low- and high-pressure phases. Eighteen slip systems (Table III) have been identified for hexagonal-close packed crystals. For the simulations only the first fifteen slip systems were modeled for the α-phase. That is,

Table I: Average Material Parameters [Vohra (1978); Fisher, et. al. (1964)]

	α-phase	ω-phase
ρ_0 (g/cm^3)	4.506	4.579
C_{11} (Mbar) : c-axis	1.7759	1.904
C_{22} (Mbar)	1.7759	1.904
C_{33} (Mbar)	1.9134	2.051
C_{12} (Mbar)	0.8757	0.938
C_{13} (Mbar)	0.8757	0.938
C_{23} (Mbar)	0.8757	0.938
C_{44} (Mbar)	0.467	0.500
C_{55} (Mbar)	0.467	0.500
C_{66} (Mbar)	0.467	0.500

Table II: Parameters for the Helmholtz Free Energy [Greeff et al. (2001)]

	a-phase	w-phase
v_0 (cm^3/g)	0.22194	0.21837
θ_0 (K)	252.0	263.4
γ_0 (1)	1.17	1.65
Γ_0 (Mbar cm^3/g K^2)	9.60334e-10	9.29019e-10
κ (1)	1.45	1.40
v^* (cm^3/g)	0.22015	0.21608
B* (Mbar)	1.1008	1.1800
B_1 (1)	4.3	3.05
ϕ_0^* (Mbar cm^3/g)	0	-1.25261e-05

Table III: a-phase slip systems (c/a = .4699 nm/.2937 nm = 1.5856)

k	$\vec{n}$	$\vec{s}$
1 Pyramidal <c+a>	[0.00, c/a, 0.866]	[0.500, -0.866, c/a]
2		[-0.500, -0.866, c/a]
3	[0.866 c/a, 0.5 c/a, 0.866]	[-0.500, -0.866, c/a]
4		[-1.00, 0.00, c/a]
5	[0.00, c/a, -0.866]	[0.500, 0.866, c/a]
6		[-0.500, 0.866, c/a]
7	[0.866 c/a, 0.5 c/a, 0.866]	[1.00, 0.00, c/a]
8		[0.500, 0.866, c/a]
9	[0.866 c/a, -0.5 c/a, 0.866]	[-0.500, 0.866, c/a]
10		[-1.00, 0.00, c/a]
11	[0.866 c/a, -0.5 c/a, 0.866]	[1.00, 0.00, c/a]
12		[0.50, -0.866, c/a]
13 Prism <a>	[0.00, 1.00, 0.00]	[1.00, 0.00, 0.00]
14	[0.866, 0.50, 0.00]	[-0.50, 0.866, 0.00]
15	[0.866, -0.50, 0.00]	[0.50, 0.866, 0.00]
16 Basal <a>	[0.00, 0.00, 1.00]	[1.00, 0.00, 0.00]
17		[-0.50, 0.866, 0.00]
18		[0.50, 0.866, 0.00]

Table IV: w-phase slip systems (c/a = .2858 nm/.4688 nm = 0.6096)

k	$\vec{n}$	$\vec{s}$
1 Basal <a>	[0.000, 0.000, 1.000]	[1.00, 0.000, 0.00]
2		[-0.50, 0.866, 0.00]
3		[0.50, 0.866, 0.00]
4 Prism <c>	[0.866, -0.500, 0.000]	[0.000, 0.000, 1.00]
5	[0.866, 0.500, 0.000]	
6	[0.000, 1.000, 0.000]	

Table V: a-phase Tensile Twin Systems: (c/a = .4699 nm/.2937 nm = 1.5856) [Bererlein and Tome (2008)]

k	$\vec{n}$	$\vec{s}$
1	[0.866, 0.50, 1.732 a/c]	[-1.00, 0.000, c/a]
2	[0.000, 1.00, 1.732 a/c]	[-0.50, -0.866, c/a]
3	[-0.866 , 0.50, 1.732 a/c]	[0.50, -0.866, c/a]
4	[-0.866, -0.50, 1.732 a/c]	[0.50, 0.866, c/a]
5	[0.000, -1.00, 1.732 a/c]	[0.50, 0.866, c/a]
6	[0.866, -0.50, 1.732 a/c]	[-0.50, 0.866, c/a]

Table VI: a-phase Compressive Twin Systems: (c/a = .4699 nm/.2937 nm = 1.5856) [Bererlein and Tome (2008)]

k	$\vec{n}$	$\vec{s}$
1	[c/a, 0.000, 1.00]	[-1.00, 0.000, c/a]
2	[0.5 c/a, 0.866 c/a, 1.00]	[-0.50, -0.866, c/a]
3	[-0.5 c/a, 0.866 c/a, 1.00]	[0.50, -0.866, c/a]
4	[-c/a, 0.000, 1.00]	[1.00, 0.000, c/a]
5	[-0.5 c/a, -0.866 c/a, 1.00]	[0.50, 0.866, c/a]
6	[0.5 c/a, -0.866 c/a, 1.00]	[-0.50, 0.866, c/a]

Table VII: Estimated Plastic Slip Parameters for the $[10\bar{1}0]$ / $[0001]$ orientation.

	a-phase	w-phase
$\dot{\gamma}_0$ (1/ms)	100 / 100	100 / 100
g_0 (Mbar)	0.0015 / 0.0115	0.0010 / 0.0115
g_l (Mbar)	0.0010 / 0.0007	0.0010 / 0.0007
g_{sat} (Mbar)	0.0035 / 0.030	0.0030 / 0.030
r	1.40 / 1.40	1.40 / 1.40
E_0 / k_B (K)	2.180e+04 / 2.180e+04	2.174e+04 / 2.180e+04
k_B / A (1/K)	1.400e-04 / 1.490e-04	1.400e-04 / 1.400e-04
p	0.6 / 0.6	0.6 / 0.6
q	1.4 / 1.4	1.4 / 1.4
h_0	0.0020 / 0.0020	0.0020 / 0.0020

Table VIII: Estimated a-phase Twinning Paramaters for the $[10\bar{1}0]$ / $[0001]$ orientation.

$\dot{\gamma}_{tw0}$ (1/ms)	0.0005 / 0.0450
a_{tw}	2.0 / 2.0
b_{tw}	3.0 / 3.0
c_{tw}	0.0 / 200.0
d_{tw}	3.0 / 3.0
γ_{tw}	0.20 / 0.20
h_{tw} (Mbar)	0.15 / 0.15
hsl (Mbar)	0.10 / 0.10
h0 (Mbar)	0.00213 / 0.00213
h_{hp} (Mbar)	100.0 / 0.0041

Table IX: Estimated Parameters for the Transformation Systems.

k	$\vec{b}$	$\vec{m}$
1	[0.500, -0.866, 0.00]	[0.1890, -0.9820, 0.00]
2	[0.500, 0.866, 0.00]	[0.1890, 0.9820, 0.00]
3	[1.000, 0.000, 0.00]	[0.9449, ,0.3273. 0.00]

for the low-pressure phase (α), three primismatic <a> and twelve pyramidal <c+a> slip systems were considered. The basal slip system was not included. Based on geometrical considerations, six slip systems were modeled in the ω- phase. They included the three basal <a> and three prismatic <c> slip systems. The six ω-phase slip systems are provided in Table IV. Atomistic simulations (Sec. III) and experimental investigations indicated that the ω-phase was relatively brittle. Also, six tensile (Table V) and six compressive twins (Table VI) [Beyerlein and Tome (2008)] for the α-phase were included in the simulations. Recall that slip within the twin systems, secondary twinning, and twinning in the ω-phase were neglected (Sec. II). Parameters for plastic slip, twinning, and phase transformation models under high-rate conditions are not available especially for high-pressure phases. For the simulations, material parameters for the inelastic deformation characteristics were estimated based on the comparisons with the impact experiments. It is recognized that there are difference slip and twin resistances [Salem et al. (2005)] for the different slip and twin systems of Ti. For example, values for the initial resolved shear stress of 37 MPa for the prismatic <a>, 47 MPa for the basal <a>, and 197 MPa for the pyramidal <c+a> have been used in the literature [Salem et al. (2005)]. However, as already suggested, values for the slip and twinning systems for high rate and pressure conditions are difficult to obtain. Therefore, uniform values for all of the slip systems and for the tensile and compressive twin systems have been used in the simulations. Also, because of the highly coupled nature of the underlying physics, it was not feasible to vary parameters for the different slip or twin systems. Consequently, the parameters for the different inelastic systems were not varied. Furthermore, the inelastic parameters were varied with the orientation of the crystal with respect to the impact direction in an effort to better match the experiments. The slip and twin model parameters are provided in Tables VII and VIII, respectively. The parameters for the shape strain tensor (Sec. III) were obtained from the atomistic simulations (Sec. IV). The habit plan normal ($\vec{m}$) and the shear direction ($\vec{b}$) are provided in Table IX. The magnitude of the shape strain tensor (γ_{tr}) was obtained knowing the volume change due to the transformation. Values for the kinetics parameter also were assumed. The parameters that were used for the transformation kinetics were $\varpi_{tr} = 3.0\,\mu s^{-1}$, $\beta_{tr} = 2.2\,x10^{-4}\,Mbar\ cm^3/g$ and $c_{tr} = 1.04$ for the [0001] orientation and $\varpi_{tr} = 1.0\,\mu s^{-1}$, $\beta_{tr} = 2.1x10^{-4}\,Mbar\ cm^3/g$, and $c_{tr} = 1.20$ for the $[10\bar{1}0]$ orientation. The amount of work that is converted into internal energy due to slip (β_{sl}) and twinning (β_{tw}) may be a function of conditions such as strain rate. For the simulations these parameters were assumed to be constant $\beta_{sl} = \beta_{tw} = 0.75$.

Comparison of the simulations and experiment for the multi-crystal experiment that was discussed in Sec. IV are provided in Figs. 8 to 10. Two orientations of the crystals with

respect to the impact direction were modeled. The comparisons in which the crystal orientations were parallel $[0001]$ and perpendicular $[10\bar{1}0]$ to the impact direction were considered. The nominal velocity of the projectile was 0.956 mm/ms, which provided a nominal peak stress of ~ 14.7 GPa. The model was implemented into an explicit, quasi-one-dimensional analysis. That is, transverse components of the velocity and stress as a function of the wave propagation direction were included. In the preliminary analyses, the Cu flyer plate was modeled using a Mie-Gruneisen equation-of-state with a polynomial representation for the Hugoniot and a Johnson-Cook strength model [Johnson and Cook (1985)]. Initial simulations of the Cu / Ti geometry were used to obtain the conditions at the impact interface. For convenience, subsequent simulations, which explored the changes in material parameters, used these results as specified velocity boundary conditions on the Ti single crystals.

A comparison of the calculated and experimental results for the free surface velocities at the back of the sample as a function of time in which the crystal was oriented along the $[0001]$ direction with respect to the wave propagation direction is provided in Fig. 8a. It may be seen from Fig. 8a that the comparison of the simulated and experimental particle velocity profiles is excellent. For the simulation, there was no slip in the ω-phase, and there was no tensile twinning. In an effort to identify which physical mechanisms that are responsible for the particle velocity response (Fig. 8a), the mass fraction of the α-phase (ξ^{α}), a curve that provides the scaled sum of the slip resistances ($\sum_{s}|\gamma|^{\alpha,s}/\gamma_{\max}$) for the α-phase, and a curve of the sum of the scaled values of the compressive twins ($\sum_{a} f^{a}/f_{\max}$) is superimposed on the scaled velocity profile through the thickness of the crystal at a time of 0.20 μs in Figs. 8b. It may be seen from Fig. 8b that the plateau for a particle velocity (Fig. 8a) of v~0.03 cm/μs is the result of combined plastic slip and twinning. The initial interpretation from the experimental data was that there was no phase transformation for this orientation. However, it may be seen from Figs. 8a and 8b that the simulation suggests that the phase transformation is initiated at a particle velocity (Fig. 8a) of about v~0.08 cm/μs. The active slip system shear strains ($\gamma_{sl}^{\alpha,k}$; $k=1,\ldots,12$) and the compressive twin volume fractions (f^{a} ; $a=1,\ldots,6$) are provided in Figs. 8c and 8d, respectively. It may be seen from Fig. 8c that all of the pyramidal <c+a> slip systems are active (k=1, … ,12). However, the three prismatic <a> slip systems (k=13,14,15) are not active. Also, all of the compressive twins (k=1, … ,6) are equally active (Fig. 8d) for this orientation.

A comparison of the calculated and experimental results for the free surface velocities at the back of the sample as a function of time in which the crystal was oriented along the $[10\bar{1}0]$ direction with respect to the wave propagation direction is provided in Fig. 9a. Again, it may be seen from Fig. 9a that the comparison of the simulated and experimental particle velocity profiles is excellent. In an effort to identify which physical mechanisms that are responsible for the particle velocity response (Fig. 9a), the mass fraction of the α-phase (ξ^{α}), curves that provide the scaled sums of the slip resistances ($\sum_{s}|\gamma|^{\alpha,s}/\gamma_{\max}$) for the α-phase and the $\omega^{k=2}$ and $\omega^{k=4}$ variants are superimposed on the scaled velocity profile through the thickness of the crystal at a time of 0.20 μs in Fig. 9b. For this orientation, there was no slip in the $\omega^{k=3}$ variant (Table III) and there were no

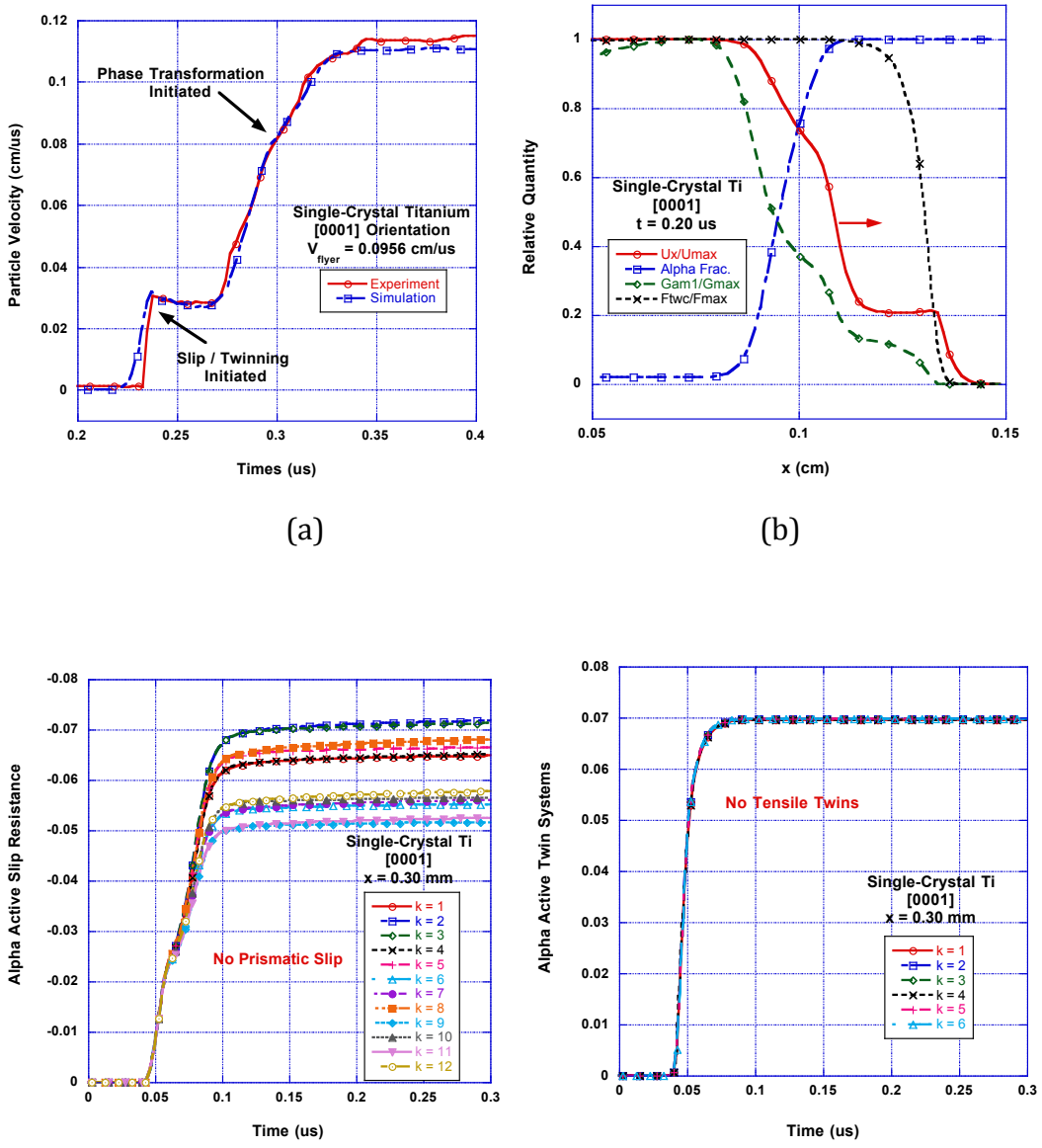

Fig. 8: Simulation of the crystal orientation [0001] with respect to the impact direction: (a) Comparison of the calculated and experimental particle velocity profiles at the back surface of the crystal. (b) Distribution of the relative velocity, a-phase volume fraction, relative slip resistance of the a-phase, and relative compressive twin volume fraction of the a-phase versus distance through the Ti single crystal at t=0.20 ms. (c) Slip resistances in the a-phase versus time at x=0.30 mm in the Ti single crystal. (d) Volume fraction of the tensile twins in the a-phase versus time at x=0.30 mm in the Ti single crystal.

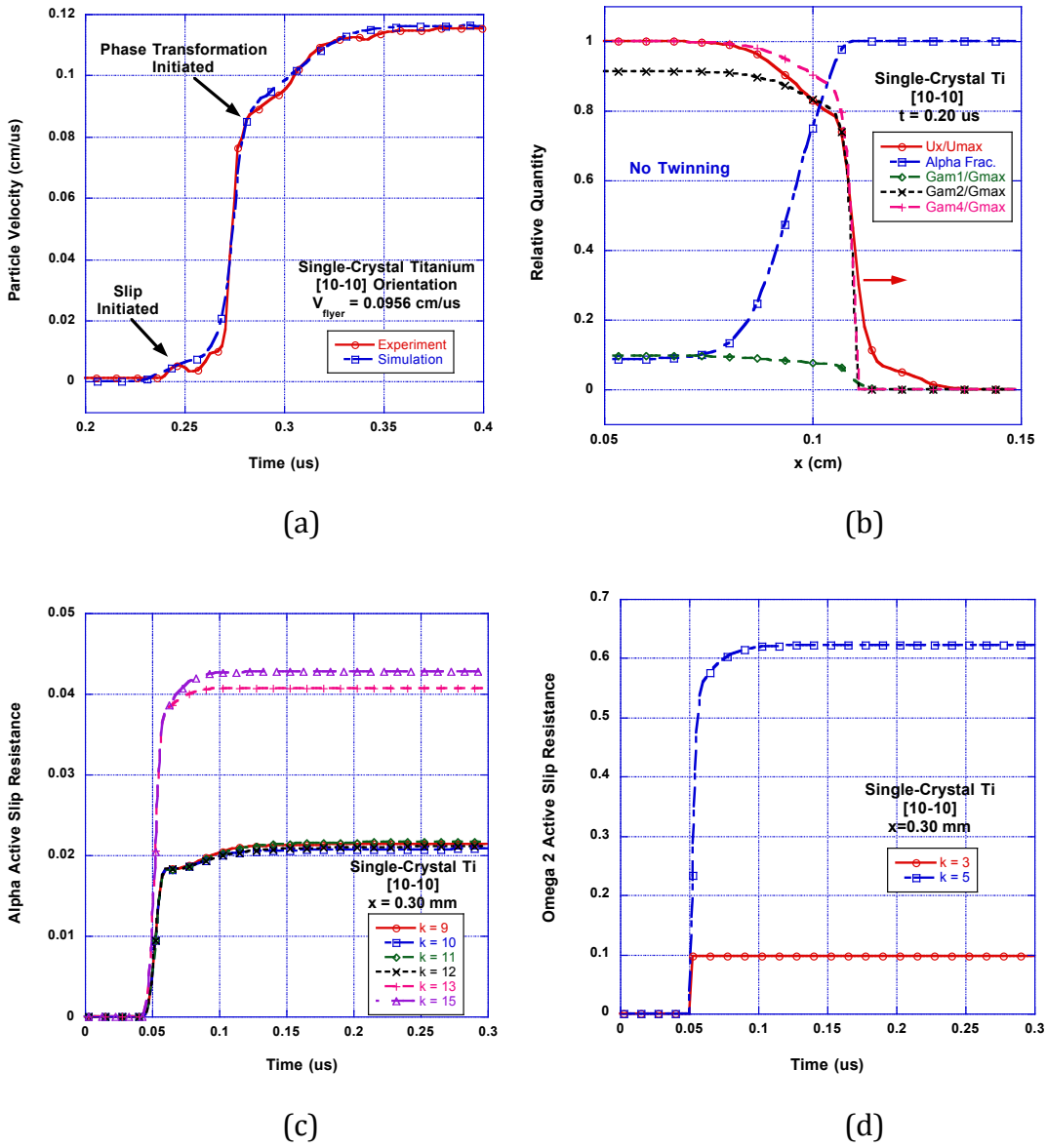

Fig. 9: Simulation of the crystal orientation $[10\bar{1}0]$ with respect to the impact direction: (a) Comparison of the calculated and experimental particle velocity profiles at the back surface of the crystal. (b) Distribution of the relative velocity, the a-phase volume fraction and the relative slip resistances of the a-phase, the w^2-variant, and the w^4-variant versus distance through the Ti single crystal at t=0.20 ms. (c) Slip resistances in the a-phase versus time at x=0.30 mm in the Ti single crystal. (d) Slip resistances in the w^2-variant versus time at x=0.30 mm in the Ti single crystal.

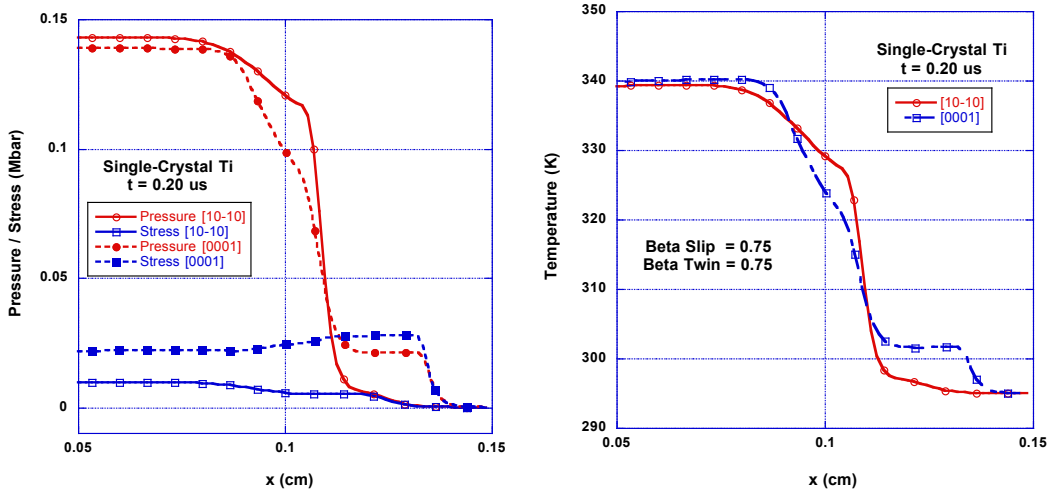

(a)

(b)

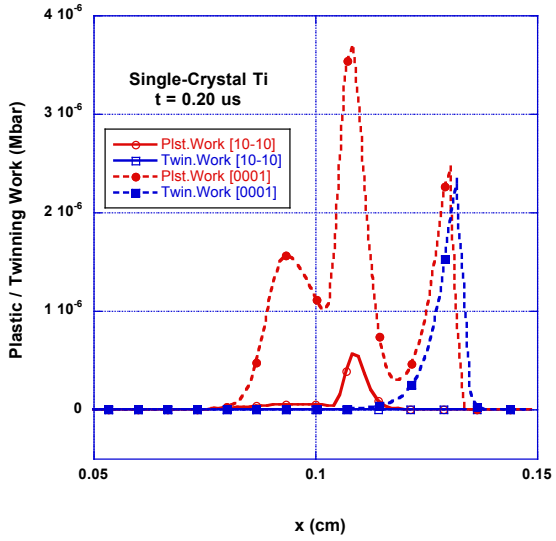

(c)

Fig. 10: Comparison of the through thickness parameters in the Ti single crystals at t-0.20 ms. (a) Pressure and von Mises Stress versus distance through the sample thickness. (b) Temperature versus distance through the sample thickness. (c) Work due to plastic slip and twinning through the sample thickness.

compressive or tensile twins. The plateau in the particle velocity profile (Fig. 9a) at v~0.005 cm/μs is a result of plastic slip in the α-phase. Also, the change in slope of the particle velocity profile (Fig. 9a) at v~0.09 cm/μs may be attributed to the α- to ω-phase transformation (Fig. 9b). It also may be seen (Fig. 9b) that the α-phase is not fully transformed for this simulation. That is, $\xi^{\alpha} \approx 0.1$ behind the compressive wave. This is a result of setting $c_{\xi} = 1.1$ in Eq. II-18. The active slip resistance for the α-phase and the $\omega^{k=2}$ variant are provided in Figs. 9c and 9d, respectively. It may be seen in Fig. 9c that slip systems k=9,10,11,12,13, and 15 (cf. Table III) are active for the α-phase. Also (Fig. 9d) slip systems k=3 and 5 (cf. Table IV) are active for the $\omega^{k=2}$ variant.

Comparisons of the stresses, temperatures, and the increments of work due to slip ($dw_{pl} = \sum_{k} \sum_{s} \dot{\gamma}^{k,s} \tau^{k,s} dt$) and twinning ($dw_{tw} = \sum_{a} \gamma_{tw} \dot{f}^{a} \tau^{a} dt$) for the two simulations is provided in Fig. 10 as a function of distance through the sample at t=0.20 μs. In Fig. 10a, curves for the average pressure and the von Mises stress for the simulations are shown. It may be seen in Fig. 10b that the temperature jump across the compression wave for the two simulations is about 45 K. Again, it should be recalled that the beta factors for slip and twinning that were used to calculate the temperatures were $\beta_{sl} = \beta_{tw} = 0.75$. For the $[0001]$ orientation, the peaks in the slip and twinning work at x~0.13 cm corresponds to the beginning of inelastic deformation (Fig. 10b). The peak in the work at about x~0.11 cm is near the end of the phase transformation. Because there is no slip or twinning in the ω-phase, the inelastic work is zero at the completion of the transformation process (x~0.08 cm). For the $[10\bar{1}0]$ orientation, there is no work due to twinning. The peak in the plastic work at x~0.11 cm occurs at the beginning of the transformation process, where slip in the ω variants increase rapidly.

Calculated information regarding the active slip and twin systems as well as the phase volume fractions may be used in the future to pursue additional high-rate experiments. Future experiments could, for example, quantify slip and twin system strain rates as well as transformation kinetics. In this manner, the resistances of the individual systems could better be determined under high-rate conditions.

VI. Summary and Discussion

A thermodynamically consistent theory, which addresses the low-rate, inelastic deformation of single crystals, was reviewed (Sec. I). The low-rate model was considered in an effort to provide a framework from which modifications and simplifications for the development of a high-rate model were made. The resulting model was intended to address the high-rate and high-pressure conditions that are encountered during impact or explosively driven deformations. The resulting thermo-mechanical, single-crystal model includes the effects of nonlinear elasticity (i.e., an equation of state), phase transformations, and plastic slip and twinning. The model is capable of investigating the high-rate response of anisotropic single-crystals and may be applied to metallic as well as molecular crystals. The development of single-crystals is important for the purpose of interpreting experiments as well as extending modeling capabilities for macro-mechanical or engineering material models. Simulations using the single-crystal model also may be used to design future

experiments for the purpose of better understanding the coupled inelastic deformations of low-symmetry crystals. Meso-mechanical models also provide a bridge between the atomistic and macro-mechanical length and time scales.

Molecular dynamics (MD) simulations were performed in an effort to investigate the response of single-crystal Ti to impact loading. The MD simulations provided insight into the phase transformation process as well as the response of the high-pressure phase of Ti. Using the MD simulations, it was determined that the Silcock orientation relationship between the low-pressure (α) and high-pressure (ω) phase was obeyed during the compression of Ti. It also was observed that the ω-phase exhibited a brittle behavior. That is, upon further loading, the ω-phase tended to revert back to the α-phase instead of deforming by plastic slip. The orientation of the habit plane between the low-pressure phase and the high-pressure variants and the specification of the shape strain tensor was facilitated by the MD investigation.

An experimental component also was included in the study. In the experiment, a multi-crystal sample of Ti was impact loaded at high-rate. A phase Doppler velocimeter (PDV) probe was attached to three of the crystals within the sample. In this manner, particle velocity histories at the back surface of three crystals, which were oriented along the $[0001]$, $[10\bar{1}0]$, and $[3\bar{1}44]$ directions with respect to the loading axis, were measured. Different particle velocity histories were obtained when the crystals were aligned with the compression axis as opposed to transverse to the compression axis. The measurements transverse to the impact direction exhibited the classical Hugiont Elastic Limit (HEL) and a phase transformation signature that are typically observed in polycrystal Ti experiments. However, when loaded along the c-axis, a significantly higher and broader HEL was observed. Also, initial observations suggested that there was no transformation signature when the crystal was shocked along the c-axis.

Comparisons were made between the model and the multi-crystal, plate impact experiments. Only the initial compression wave was considered in both the simulations and the experiment. The comparisons were made with the particle velocity at the back surface of the multi-crystal target. It was shown that the model was able to capture the features of the deformation for the crystals that were oriented along the $[0001]$ and $[10\bar{1}0]$ direction with respect to the loading axis. The simulations highlighted the coupled effects of the physical phenomena under consideration. Consequently, details of the *in situ* response of the material with respect to the plastic slip, twinning, and transformation processes were inferred. Issues related to the degree of twinning or transformation cannot be quantified from these far-field measurements. In the future detailed *in situ* experimental investigations are being planned. Once the details of the *in situ* processes are understood, better models for the free energies, transformation kinetics, plastic slip resistances, and twinning, for example, may be pursued. The model that has been developed requires a number of parameters to characterize the effects of nonlinear, inelastic response. In general, these parameters are not readily available for high-rate and high-pressure applications. Consequently, an effort was not invested in obtaining a uniform set of parameters for the two simulations. Instead, a different set of parameters was applied for the two orientations. Furthermore, the differences in the resistances of the slip and twin systems were not pursued. It is felt that additional high rate, single-crystal data is necessary to quantify these differences.

Improvements related to the numerical implementation of the model also should be given future consideration. These include improving the degree of implicitness or temporal subcycling [Dumoulin et al. (2009); Ling et al. (2005)] of the constitutive model within regions of large gradients. The existing explicit implementation requires small time step sizes ($\Delta t \sim 10^{-5}\ \mu s$). A thermally activated plasticity model was used in the development. For high-strain rates ($\dot{\varepsilon} > 10^{4}\ s^{-1}$) the growth of dislocation generation begins to accelerate, which leads to an abrupt increase in the dislocation density and results in the rapid increase in the material flow stress. Consequently, future improvements to the model should include a dislocation drag plastic slip model. A dislocation density based approach also should be considered. However, the physics of dislocation generation at high strain-rates represents an area that will require future research.

The effects of transformations, plasticity, twinning, and damage provide important coupled processes on the stress-strain response of materials subjected to shock loading conditions. Future efforts will consider the effects of damage [Lu et al. (2004)] on the response of high-rate material deformation. Continuum damage mechanics models for single crystals offer a convenient approach. An existing approach models damage by degrading the elastic stiffness through a damage volume fraction for each constituent [Suiker et. al. (2007a); Suiker et. al. (2007b)]. A kinetic law for the damage volume fractions is provided in terms of driving forces for damage. These driving forces are provided using thermodynamically consistent considerations. This approach reflects a brittle-like behavior of the material. A single-crystal, ductile damage approach [Lu et. al. (2004)], which includes softening of the plastic velocity gradient, will be considered. This approach offers the potential for modeling spall effects in single crystals.

Improved expression for the free energies also must be developed. The existing model relies on an extension to the Helmholtz free energy in an effort to include nonlinear elasticity. Also a Gibbs free energy, which is a function of uniform pressure and temperature, was used in the expression for the transformation kinetics. Consequently, the three high-pressure variant of Ti were produced equally. More general transformation driving forces that are written in terms of the total stress or strain tensor should be considered. Improved expressions for the free energies also should include the effects of the energy barriers between phases. In this manner, transformation hysteresis or retained high-pressure phase for the unloading path could be modeled better.

Acknowledgements:

This effort was supported by Campaign 2 under the direction of R.L. Martineau, G.T. Gray III, D. M. Dattelbaurm, and R.T. Olson, the DOE Advanced Simulation and Computing (ASC) Program under the direction of M.W. Schraad and D.L. Preston, the Joint Department of Energy (DOE), and the program for Materials-Radiation Interaction in the Extreme (MaRIE) under the direction of J.L. Sarrao. The support of these programs is appreciated. Discussions with H. Mourad also are appreciated.

References:

Ball, J.M. and James, R.D. (1987) Fine phase mixtures as minimizers of energy. Arch. Ration. Mech. Anal. **100** (1): 13-52

Barton, N.R., Benson, D.J., Becker, R. (2005) Crystal level continuum modeling of phase transformations: the α–ε transformation in iron. Modelling Simul. Mater. Sci. Eng. **13**. 707-731.

Barton, N.R., Wenke, H-R. (2007) Dauphine twinning in polycrystalline quartz. Modelling Simul. Mater. Sci. Eng. **15**. 369-384.

Becker, R. (2004) Effects of crystal plasticity on materials loaded at high pressures and strain rates. Int. J. Plast. **20**, 1983-2006.

Beyerlein, I.J., Tome, C.N. (2008) A dislocation-based constitutive law for pure Zr including temperature effects. Int. J. Plast. **24**:867-895.

Bhattachary, K. (2007) Microstructure of martensite: why it forms and how it gives rise to the shape-memory effect. Oxford Series on Materials Modelling. Oxford University Press, Oxford, UK.

Bonet, J. and Wood, R.D. (1997) Nonlinear continuum mechanics for finite element analysis, Cambridge University Press, 40 West 20th St, New York, NY, USA

Bronkhorst, C.A., Hansen, B.L., Cerreta, E.K., Bingert, J.F. (2007) Modeling the microstructural evolution of metallic polycrystalline materials under localization conditions. J. Mech. Phys. Solids. **55**:2351-2383.

Cerreta, E.K., Escobedo, J.P., Rigg, P.A., Trujillo, C.P., Brown, D.W., Sisneros, T.A. Clausen, B., Lopez, M.F., Lookman, T., Bronkhorst, C.A., Addessio, F.L. (2013) The influence of phase and substructural evolution during dynamic loading on subsequent mechanical properties of zirconium. Acta Materialia. **61**: 7712-7719.

Clayton, J.D., Becker, R. (2012) Elastic-plastic behavior of cyclotrimethylene trinitramine single crystals under spherical indentation: modeling and simjulation. J. Appl. Phys. **111**, 063512, 1-9.

De, S. and Rahul, A.R. Z. (2014) A fully anisotropic single crystal model for high strain rate loading conditions with an application to a-RDX, J. Mech. Phys. Solids **64**; 287-301.

Dumoulin, S., Hopperstad, O.S. and Berstad, T. (2009) Investigation of integration algorithms for rate-dependent crystal plasticity using explicit finite element codes. Compt. Mat. Sci. **46**, 785-799.

Fisher, E.S. Renken, C.J. (1964) Single-Crystal elastic moduli and the hcp-bcc transformation in Ti, Zr, Hf. Phys. Rev. **135**:2A. A482-A494.

Greeff, C.W. (2005) Phase changes and the equation of state of Zr. Modelling Simul. Mater. Sci. Eng. **13**:1015-1027.

Greeff, C.W., Trinkle, D.R., Albers, R.C. (2001) Shock-induced α–ω transition in titanium. J. Appl. Phys. **90**:5, 2221-2226.

Greeff, C.W., Trinkle, D.R. and Albers, R.C. (2002) Alpha-Omega Transition in Ti: Equation of state and kinetics. In shock Compression of Condensed Matter-2001, M.D. Furnish, N.N. Thadhani and Y. Horie eds. AIP (Melville 2002) 225-228.

Hennig, R.G., Lenosky, T.J., Trinkle, D.R., Rudin, S.P. and Wilkins, J.W. (2008) Classical potential describes martensitic phase transformations between the α, β, and ω titanium phases, Phys. Rev. B, **78**: 054121.

Ivanisenko, Y, Kilmametov, A, Rosner, H and Valiev, RA (2008) Evidence of α-ω phase transition in titanium after high pressure torsion. Int. J. Mat. Res. **99**:1 36-41.

James, R.D. and Hane, K.F. (2000) Martensitic transformations and shape-memory materials. Acta Mater. **48** (1); 197-222.

Jaworski, A. and Ankem, S. (2005) Influence of the ω phase on the tensile and creep deformation mechanisms of α–β titanium alloys. Rev. Adv. Mater. Sci. **10**: 11-20.

Johnson, G.R. and Cook, W.H. (1985) Fracture characteristics of three metals subjected to various strains, strain rates, temperatures, and pressures, Eng. Frac. Mech. **21**,1;31-48.

Jyoti, G., Tewari, R., Joshi, K.D., Srivastava, D., Dey, G.K., Gupta, S.C., Sikka, and S.K., Banerjee, S. (2008) Alpha to omega transition in shocked compressed Zr: Crystallographic Aspects. Defect and Diffusion Forum, **279**; 133-138.

Kalidindi, S.R., Bronkhorst, C.A., Anand, L. (1992) Crystallographic texture evolution in bulk deformation processing of fcc metals. J. Mech. Phys. Solids. **40**:3, 537-569.

Kalidindi, S.R. (1998)Incorporation of deformation twinning in crystal plasticity models. J. Mech. Phys. Solids, **46**, 2, 267-290.

Ling, X., Horstemeyer, M.F., Potirniche, G.P. (2005) On the numerical implementation of 3D rate-dependent single crystal plasticity formulations. Int. J. Numer. Meth. Engng. 63:548-568.

Lu, T., Guang, Z., Ke-shi, Z., Xu, J.Q., Hai-dong, Y. (2004) On analysis of the elasto-viscoplastic response of single crystals with anisotropic damage: constitutive modeling and computational aspects. Int. J. Numer. Meth. Engng. **61**:406-432.

Luscher, D.J., Addessio, F.L., Cawkwell, M.J. and Ramos, K.J. (2016) A dislocation density-based continuum model of the anisotropic shock response of single-crystal α-RDX (in preparation).

Luscher, D.J., Bronkhorst, C.A., Alleman, C.N., Addessio, F.L. (2013) A model for finite-deformation nonlinear thermomechanical response of single crystal copper under shock conditions. J. Mech. Phys. Solids. **61**: 1877-1894.

Marsh, S.P. (1980) LAS shock Hugoniot data. University of California Press, Los Angeles, CA.

Mescheryakov, Y I and Divakov, A K (2001) Affect of shock-induced phase transformation on dynamic strength of titanium alloys. Int. J. Impact Eng. **26** 497-508.

Meyers, M.A. (1994) Dynamic behavior of materials, Wiley-Interscience publication, New York, NY USA.

Morrow, B.M., Lebensohn, R.A., Trujillo, C.P., Martinex, D.T., Addessio, F.L., Bronkhorst, C.A., Lookman, T. and Cerreta, E.K. (2016) Characterization and modeling of mechanical behavior of single crystal titanium deformed by split-Hopkinson pressure bar, I. J. Plasticity **82**;225-24 0.

Plimpton, S. (1995) Fast parallel algorithms for short-range molecular dynamics. J. Comp. Phys; **117**; 1-19.

Salem, A.A., Kalidindi, S.R., Semiatin, S.L. (2005) Strain hardening due to deformation twinning in α-titanium: constitutive relations and crystal-plasticity modeling. Acta Materialia. **53**. 3495-3502.

Singh, A K, Mohan, M and Divakar C (1982) The kinetics of pressure-induced α-ω transformation in Ti. J. App. Phys. 531221-1223.

Suiker, A.S.J. and Turteltaub, S. (2005) Computational modeling of plasticity induced by martensitic phase transformations. Int. J. Num. Meth. Engng. **63**:1655-1693.

Suiker, A.S.J. and Turteltaub, S. (2007a) Numerical modeling of transformation-induced damage and plasticity in metals. Modelling Simul. Mater. Sci. Eng. **15**: S147-S166.

Suiker, A.S.J Turteltaub, S. (2007b) Crystalline damage growth during martensitic phase transformations. Phil. Mag. **87**:32, 5033-5063.

Tjahjanto, D.D., Turteltaub, S., Suiker, A.S.J. (2008a) Crystallographically based model for transformation-induced plasticity in multiphase carbon steels. Continuum Mech. Thermodyn. **19**: 399-422.

Tjahjanto, D.D., Turteltaub, S., Suiker, A.S.J., van der Zwaag, S. (2008b) Transformation-induced plasticity in multiphase steels subjected to thermomechanical loading. Phil. Mag. **88**:28, 3369-3387.

Turteltaub, S., Suiker, A.S.J. (2006) A multiscale thermomechanical model for cubic to tetragonal martensitic phase transformations. Int. J. Solids Struct. **43**: 4509-4545.

Vohra, Y.R. (1978) Kinetics of phase transformations in Ti, Zr, Hf, under static and dynamic pressures, J. Nucl. Mater. **75**: 288-293.

Winey, J.M.and Gupta, Y.M. (2004) Nonlinear anisotropic description for shocked single crystals: Thermoelastic response and pure mode wave propagation. J. Appl. Phys. **99**:4, 1993-1999.

Winey, J.M. and Gupta, Y.M. (2006) Nonlinear anisotropic description for the thermomechanical response of shocked single crystals: inelastic deformation. J. Appl. Phys. **99**: 023510, 1-11.

Winey J.M. and Gupta, Y.M. (2010) Anisotropic material model and wave propagation simulations for shocked pentaerythritol tetranitrate single crystals. J. Appl. Phys. **107**, 103505.

Young, D.A. (1991) Phase diagrams of the elements, University of California Press, Berkeley and Los Angeles, CA, USA.

Zong, H., Ding, X., Lookman, T., Li, J., Sun, J., Cerreta, E.K., Escobedo, J.P., Addessio, F.L, and Bronkhorst, C.A. (2014a) Collective nature of plasticity in mediating phase transformation under shock, Phys. Rev. B **89**; 220101.

Zong H, Lookman, T, Ding, X, Luo, S-N and Sun, J (2014b) Anisotropic shock response of titanium: Reorientation and transformation mechanisms. Acta Mater. **65**, 10-18.